2-8-2018

Direct Numerical Simulation of Transverse Ripples: 1. Pattern Initiation and Bedform Interactions

Nadim Zgheib

J. J. Fedele

D. C. J. D. Hoyal

M. M. Perillo

S. Balachandar

AGU PUBLICATIONS

JGR

Journal of Geophysical Research: Earth Surface

RESEARCH ARTICLE
10.1002/2017JF004398

This article is a companion to Zgheib et al. (2018) https://doi.org/10.1002/2017JF004399.

Key Points:
- Mesoscale resolved simulations show the different mechanisms for bedform-bedform interactions to be very similar to each other
- Similar to laminar flows over dunes and ripples, a positive phase shift is observed between bed shear stress and topology even in mesoscale-resolved turbulent flow field
- Simulations match Coleman and Melville (1996) theory on bedform initiation from a flat bed

Correspondence to:
N. Zgheib,
nadim.zgheib@lau.edu.lb

Citation:
Zgheib, N., Fedele, J. J., Hoyal, D. C. J. D., Perillo, M. M., & Balachandar, S. (2018). Direct numerical simulation of transverse ripples: 1. Pattern initiation and bedform interactions. *Journal of Geophysical Research: Earth Surface*, *123*, 448–477. https://doi.org/10.1002/2017JF004398

Received 15 JUN 2017
Accepted 29 JAN 2018
Accepted article online 8 FEB 2018
Published online 9 MAR 2018

Direct Numerical Simulation of Transverse Ripples: 1. Pattern Initiation and Bedform Interactions

N. Zgheib[1,2], J. J. Fedele[3], D. C. J. D. Hoyal[3], M. M. Perillo[3], and S. Balachandar[1]

[1]Department of Mechanical and Aerospace Engineering, University of Florida, Gainesville, FL, USA, [2]School of Engineering, Lebanese American University, Byblos, Lebanon, [3]ExxonMobil Upstream Research Company, Houston, TX, USA

Abstract We present results of coupled direct numerical simulations between flow and a deformable bed in a horizontally periodic, turbulent open channel at a shear Reynolds number of $Re_\tau = 180$. The feedback between the temporally and spatially evolving bed and the flow is enforced via the immersed boundary method. Using the near-bed flow field, we provide evidence on the role of locally intense near-bed vortical structures during the early stages of bed formation, from the emergence of quasi-streamwise streaks to the formation of incipient bedform crestlines. Additionally, we take a new look at a number of defect-related bedform interactions, including lateral linking, defect and bedform repulsion, merging, and defect creation, and show that the underlying mechanisms, in these flow-aligned interactions, are very similar to each other. Consequently, the interactions are labeled differently depending on the geometry of interacting structures and the outcome of the interaction. In the companion paper, we compare our results to published experimental data and provide an extensive quantitative analysis of the bed, where we demonstrate the importance of neighboring structures, especially upstream neighbors, on bedform dynamics (growth/decay and speed) and wave coarsening. Video files of bed evolution are available in the supporting information.

1. Introduction

Bedforms are fascinating features of deformable sediment beds that evolve under the action of an overlying flow field. They are present in unidirectional (e.g., Best, 1992; Gyr & Schmid, 1997) and oscillatory (e.g., Bagnold & Taylor, 1946; Ribberink & Al-Salem, 1994) configurations and may develop under laminar (e.g., Charru & Mouilleron-Arnould, 2002; Charru et al., 2013; Ouriemi et al., 2009a) or turbulent regimes (e.g Best & Kostaschuk, 2002; Ouriemi et al., 2009b). They are present in subaqueous (e.g., Ashley, 1990) and aeolian (e.g., Wilson, 1972) environments as well as in various atmospheric conditions on different planets (e.g., Breed et al., 1979; Howard, 2007). Depending on certain parameters such as sediment availability, grain Reynolds number, Froude number, flow depth, and flow intensity, a rich variety of bedforms develop, including ripples (e.g., Nielsen, 1981), dunes (e.g., Nelson & Smith, 1989), antidunes (e.g., Kennedy, 1969), and cyclic steps (e.g., Kostic et al., 2010; Smith et al., 2013). Field studies have shown a large range of scales from tiny ripples of the order of millimeters to massive dunes stretching for kilometers. Bedforms are therefore a key feature of many sediment-flow systems and thus have been extensively researched over the past several decades.

Many researchers suggest self-organization (Baas, 1993, 2007; Coco & Murray, 2007; Kocurek et al., 2010; Werner, 1995, 1999, 2003) as a possible explanation to the emergence of bedform patterns. Indeed, while interactions at the microscale level between individual grains and the surrounding fluid are an essential feature of this multiphase phenomenon, such interactions are especially important in the very early stages of bed development, when the bed is still featureless, and the feedback from the bed to the flow is relatively weak. As small sediment piles begin to emerge from a relatively flat bed (Coleman & Melville, 1996), they collectively interact with the flow and with each other through the flow, and overshadow isolated grain-fluid interactions (Kocurek et al., 2010). Werner (2003) suggested that the microscale interactions at the grain level become "slaved" to the larger scale bedform-flow and bedform-bedform interactions. Additionally, Kocurek et al. (2010) argue that once bedform patterns arise, the overlying flow and the sediment transport become functions of bed morphology. In other words, details of the flow field are not necessary for a leading order description of bed dynamics (Jerolmack & Mohrig, 2005).

The self-organized aspect of bedforms has motivated modeling approaches that primarily focus on bedform-flow and bedform-bedform interactions and disregard the effects of the flow field (Jerolmack & Mohrig, 2005; Landry & Werner, 1994; Stam, 1997; Werner, 1995). Jerolmack and Mohrig (2005) developed a

two-dimensional anisotropic model for subaqueous bedform dynamics, in which they used the height and slope of bedforms to approximate the bed shear stress. Their model was suitable to provide a description of bedform initiation, evolution, and long-time behavior. They followed a deterministic and a stochastic (by adding small-amplitude white noise) approach and were able to produce a variety of dynamical behavior observed in laboratory experiments and field studies. The model consisted of a few adjustable parameters that could be potentially computed from laboratory experiments and direct numerical simulations. The model was, however, not sensitive to the values of these parameters and showed robustness in the sense that pattern formation was present for a wide range of parameters. Their initial model, however, lacked the bedform-bedform coupling necessary for bedform interactions. Later models (Swanson et al., 2016) based on Jerolmack and Mohrig (2005) showed capability in reproducing certain defect-related interactions such as lateral linking, defect and bedform repulsion, and merging.

Up until recently, numerical simulations of pattern formation under a shearing flow field (e.g., Charru et al., 2016; Giri & Shimizu, 2006; Kidanemariam & Uhlmann, 2014, 2017; Niemann et al., 2010; Sotiropoulos & Khosronejad, 2016) have received very little attention, whereas field studies (e.g., Kostaschuk, 2000; Kocurek et al., 2010) and experiments (e.g., Baas, 1994; Coleman & Melville, 1996; Venditti et al., 2005) coupled with theoretical investigations (e.g., Colombini, 2004; Engelund, 1970; Hino, 1968; Kennedy, 1969) have been the primary methods by which these patterns were studied. For large structures, or under extremely turbulent flow conditions, field observations usually constitute the only source of data due to the difficulties in generating such conditions in a laboratory setting. Laboratory experiments on the other hand provide a more controlled environment that allows for more precise measurements albeit for more moderate flow conditions and manageable bedform dimensions. Additionally, contrary to most field studies, laboratory experiments provide the possibility to track the temporal evolution of bedforms through various stages of development. However, when the tracked phenomena have very small length scales of the order of a few grain diameters, or when they occur within a very short time span of a few seconds, as in the early stages of bed development, even laboratory measurements become challenging.

Recent developments in numerical methods have made it possible to study different aspects of bed morphology and have shown great potential in reproducing key bedform interactions observed in field studies and laboratory experiments. Kidanemariam and Uhlmann (2017) have recently conducted direct numerical simulations, with over one million finite size particles, to study pattern formation in subaqueous sediment with a fully resolved flow field around individual grains. They used a channel flow configuration where they varied the streamwise length of the domain and showed that there exists a minimal streamwise dimension, between 75 and 100 grain diameters, below which patterns did not evolve and the sediment bed remains nearly flat. They also observed the volumetric flux of particles and the mean bed shear stress to increase with increasing ripple size; nevertheless, they find the relationship between the two to be sufficiently described by the modified Meyer-Peter and Müller (1948) bedload relation of Wong and Parker (2006).

These fully resolved simulations have provided a wealth of data but are computationally very expensive. Recent modeling efforts have focused on an Eulerian Lagrangian framework to model the flow and the particle bed (e.g., Nabi et al., 2013; Sun & Xiao, 2016). Other coupled flow-particle numerical approaches resolve the flow field, through detached-eddy, large-eddy, or direct numerical simulation, and model the bed using the Exner equation (Chou & Fringer, 2010; Escauriaza & Sotiropoulos, 2011; Khosronejad et al., 2011; Sotiropoulos & Khosronejad, 2016). To lower the computational cost of the simulations, the grid may be chosen to be fine enough to resolve the flow, but large enough to accommodate a number grains within a grid cell, which results in coarse graining. Additionally, a boundary-fitted curvilinear coordinate system may be applied such that the lower boundary of the domain follows exactly the evolving flow-sediment interface (Chou & Fringer, 2010). Or alternatively, a fixed mesh with an immersed boundary (Uhlmann, 2005) may be used to track the evolution of the bed (Khosronejad et al., 2011; Sotiropoulos & Khosronejad, 2016). In the present work, we use the latter approach in which the flow field is solved on a fixed Eulerian mesh, and the bed is tracked using Lagrangian markers, which define the immersed boundary.

The purpose of this study is first to show the capability of our simulations by reproducing key features of bed morphology under a turbulent unidirectional flow. Specifically, we are able to reproduce the patterns of ripple formation at the various stages of development, starting from a flat bed, as well as many of the interactions that occur during bed evolution. Using the near-bed flow field, we provide evidence on the role of locally intense vortical structures during the early stages of bed formation, from the emergence of quasi-

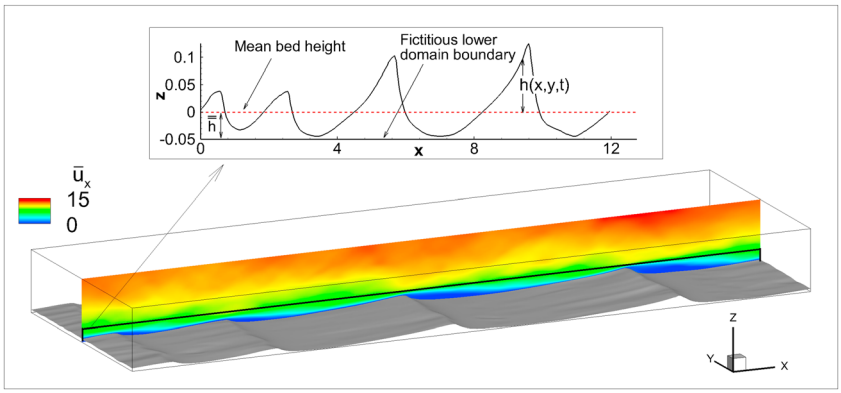

Figure 1. Numerical domain showing iso-contours of the span averaged streamwise component of the velocity $\overline{u}_x$ on top of an erodible, spatially and temporally evolving bed surface. Flow is from left to right. Inset: Cross-sectional slice of the domain midway in the spanwise direction. The dashed red line corresponds to the mean bed height, from which the time-dependent bed elevation $h(x, y, t)$ is measured.

streamwise streaks to the formation of incipient crestlines. Additionally, we take a new look at a number of defect-related bedform interactions, including lateral linking, defect and bedform repulsion, merging, and defect creation, and show that the mechanisms that control the underlying fluid mechanical interactions are very similar, and that interactions are labeled differently depending on the geometry of interacting structures and the outcome of the interaction. The simulations also provide the opportunity to test theories regarding the generation of initial bed waves, such as that of Coleman and Melville (1996) in which they hypothesized that sediment pattern evolution from an initially flattened bed is initiated by the occurrence of small sediment pileups, which grow and generate additional pileups further downstream at a preferred spacing. The main objective of this work is to perform turbulence-resolved simulations and use the results to relate the dynamics of near-bed vortical structures to shear-induced bedload transport and then to the generation and interaction of bedforms.

The remainder of this paper is organized as follows. In section 2, we layout the mathematical model and briefly discuss the steps taken in evolving the deformable bed. In section 3, we perform a validation case of flow over a wavy wall. In section 4, we describe the different stages of ripple formation and elaborate on many of the bedform interactions present in our simulations. A closer look at the early stages of bed formation is explored in section 5, where we examine the spatiotemporal evolution of an isolated sand pileup on an initially flattened bed. Finally, discussion and conclusions are presented in sections 6 and 7, respectively.

In the companion paper (Zgheib et al., 2018), referred to hereafter as Paper 2, we compare our results to published experimental data and provide an extensive quantitative analysis of the bed, where we demonstrate the importance of neighboring structures, especially upstream neighbors, on bedform dynamics (growth/decay and speed), and wave coarsening. We also provide a quantitative analysis on ripple self-similarity and examine ripple properties such as bedform spectra, Fourier expansions, and two-point correlations.

2. Mathematical Model

The present configuration is that of a coupled bed flow simulation, in which the flow field is obtained by integrating (1) and (2), the conservation equations of mass and momentum, respectively, using a pseudo spectral code (Cantero et al., 2007; Cortese & Balachandar, 1995; Shringarpure et al., 2012). The bed is evolved using the Exner equation (3) (Ancey, 2010; Cayocca, 2001; Paola & Voller, 2005), whose input, the volumetric flux of sediment, is obtained from the flow-induced shear stress at the bottom boundary of the fluid domain as defined by the bed. The time evolving bed is imposed as the bottom boundary of the fluid domain using the immersed boundary method (IBM) of Uhlmann (2005) (also see Akiki & Balachandar, 2016). The equations are solved inside a rectangular channel as seen in Figure 1.

$$\nabla \cdot \boldsymbol{u} = 0, \tag{1}$$

$$\frac{D\boldsymbol{u}}{Dt} = \boldsymbol{e}_x - \nabla p + \frac{1}{\mathrm{Re}_\tau}\nabla^2 \boldsymbol{u} + \boldsymbol{f}, \tag{2}$$

$$\varphi \frac{\partial h}{\partial t} = -\nabla \cdot \boldsymbol{q} + \varepsilon |\boldsymbol{q}| \nabla^2 h, \tag{3}$$

Here $\boldsymbol{u}$ represents the three-dimensional flow field, $\boldsymbol{e}_x$ represents the unit nondimensional mean streamwise pressure gradient, p is the deviation from the mean pressure within the domain, and $\boldsymbol{f}$ is the coupling force in the IBM that must be applied to enforce the no-slip boundary condition at the bed. The φ is the sediment volume fraction in the bed, given here a value of $\varphi = 0.6$ (note that $1 - \varphi$ is the porosity of the bed). The sediment bed height with reference to the mean is denoted by h, where the mean bed height corresponds to a completely flat bed. The volumetric flux of sediment is $\boldsymbol{q}$, and $\varepsilon = 4$ is an adjustable parameter that controls the numerical diffusion term. We have adopted the same value of ε used in previous studies as it was shown to provide realistic results in terms of bed topology (Bertin et al., 2009; Cayocca, 2001; Guérin et al., 2016). Our simulations indicate that bed evolution is not very sensitive to the exact value of ε provided it remains in the range $3 \lesssim \varepsilon \lesssim 5$.

The morphodynamic aspect of the study, as will be discussed below, considers a coarse graining approach where each grid cell corresponds to a sediment volume at the mesoscale. The purpose of the diffusion term in (3) is to dampen numerical high-frequency fluctuations.

Variables most frequently used in the paper are included in Table 1 for easier referencing. Throughout the manuscript, dimensional quantities will be denoted by an asterisk. All other variables are to be taken as nondimensional unless stated otherwise. The length scale is the mean height of the channel above the mean bed elevation, that is, the mean flow depth, H_f^*. The average shear velocity on the initially flattened bed, U_τ^*, is the velocity scale, and the corresponding pressure scale $\rho_f^* U_\tau^{*2}$ results in a nondimensional streamwise pressure gradient of unity. The ratio $T^* = H_f^*/U_\tau^*$ represents the time scale. The shear Reynolds number Re_τ is defined as

$$\mathrm{Re}_\tau = \frac{U_\tau^* H_f^*}{\nu^*}, \tag{4}$$

where ν^* is the kinematic viscosity of the fluid.

Fourier expansions are used in the horizontal streamwise and spanwise x and y directions, respectively, which necessitates the use of periodic boundary conditions. Chebyshev polynomials are used in the vertical z direction with free-slip boundary condition at the top of the computational domain. The bottom boundary of the computational domain is a fictitious boundary that lies below the bed where no-slip boundary condition is imposed (see Figure 1 where the rippled bed can be seen to be located above the bottom plane of the computational box). The details of this boundary condition are not important since appropriate boundary conditions (no slip and no penetration) are enforced at the bed using the immersed boundary condition. Additionally, because of the no penetration condition, the permeability of the sediment bed has been neglected.

Details of the numerical simulations are provided in Table 2. The flow is fully resolved only in the sense that the grid resolution is fine enough to capture the smallest Kolmogorov flow scales, but does not resolve the flow around the individual sediment grains. The resolution of $288 \times 96 \times 301$ grid points along the streamwise, spanwise, and vertical directions may appear to be a resolution overkill with the current Fourier-Fourier-Chebyshev spectral methodology for $Re_\tau = 180$. While this may be true for turbulent flow over a smooth wall, the much finer grid is chosen in anticipation of pattern growth on the bed. We require the turbulent flow to be fully resolved even when the bed takes a complex form consisting of many ripples and crestlines. Furthermore, the increased resolution is required in the context of the IBM. For example, with the present resolution, the simulation of flat bed turbulence using IBM is able to recover the turbulent open channel flow statistics.

As we will observe, intense turbulent shear layer vortices form on the downstream side of tall ripples and a fine grid is required to resolve these vortical structures. The grid resolution along the x and y directions is, however, large enough to accommodate a small sediment volume, which results in coarse graining. Additionally, the immersed boundary, which represents the sediment-fluid interface, is composed of $N_x \times N_y$ Lagrangian markers where the zero velocity (no-slip and no-penetration) condition is enforced. The x and y coordinates of these markers coincide with the underlying Eulerian mesh, and their vertical position varies as the bed deforms due to the overlying flow.

Table 1
Symbols, Notation, and Nomenclature Definition

Variable/notation	Symbol	Mathematical expression/definition
	Scaling variables	
Mean flow depth (length scale)	H_f^*	-
Mean shear velocity (velocity scale)	U_τ^*	-
Time scale	T^*	H_f^*/U_τ^*
	Flow-related variables	
3D velocity field	$\boldsymbol{u}$	
Perturbation pressure	p	
Numerical domain size (streamwise × spanwise × vertical)	$L_x \times L_y \times L_z$	-
Numerical resolution	$N_x \times N_y \times N_z$	-
Bulk velocity	U_b	$\frac{1}{L_y H_f}\int_0^{L_y}\int_0^{H_f} u dz dy$
Fluid density	ρ_f^*	-
Gravitational acceleration	g^*	-
Fluid kinematic viscosity	ν^*	-
Fluid dynamic viscosity	μ^*	-
Particle Reynolds number	Re_p	$\frac{1}{\nu^*}\sqrt{\frac{\rho_p^*-\rho_f^*}{\rho_f^*} g^* d_p^{*3}}$
Shear Reynolds number	Re_τ	$U_\tau^* H_f^*/\nu^*$
	Bed-related variables	
Bed shear stress	τ^*	$\left(\frac{\mu^* U_\tau^*}{H_f^*}\right)\frac{\partial u}{\partial n}$
Shields number	Θ	$\tau^*/\left[\left(\rho_p^*-\rho_f^*\right) g^* d_p^*\right]$
Critical Shields number	Θ_{cr}	$\frac{1}{2}\left[0.22\ \mathrm{Re}_p^{-0.6} + 0.06\ \exp\left(-17.77\ \mathrm{Re}_p^{-0.6}\right)\right]$
Volumetric flux of sediment per unit width[a]	q	$\left(\mathrm{Re}_p/\mathrm{Re}_\tau\right) c_1 (\Theta - \Theta_{cr})^{c_2}$
Bed volume fraction	φ	1 − porosity
Diffusion coefficient	ϵ	-
Bed elevation (with respect to mean)	h	-
Mean bed height	$\overline{h}$	-
Sediment diameter	d_p^*	-
Sediment density	ρ_p^*	-
	Notation	
Unit vector	$\boldsymbol{e}$	
x, y, z, bed-tangent, bed-normal components of quantity ■	$\{\blacksquare_x, \blacksquare_y, \blacksquare_z, \blacksquare_t, \blacksquare_n\}$	
Time average of quantity ■	$\langle\blacksquare\rangle$	$\frac{1}{T}\int_{t_1}^{t_1+\psi}\blacksquare dt$
Spanwise average of quantity ■	$\overline{\blacksquare}$	$\frac{1}{L_y}\int_0^{L_y}\blacksquare dy$
Stream and span average of quantity ■	$\overline{\overline{\blacksquare}}$	$\frac{1}{L_x L_y}\int_0^{L_y}\int_0^{L_x}\blacksquare dx dy$

Note. The asterisk denotes dimensional quantity.
[a]Based on the MPM (1948) modified Wong and Parker (2006) model ($c_1 = 4.93$, $c_2 = 1.6$)

Details on the implementation of the immersed boundary technique are presented in Akiki and Balachandar (2016) and are briefly addressed here. First, the velocity at each Lagrangian marker is computed through interpolation from the velocity on the surrounding Eulerian mesh. A discrete delta function ensures that the interpolation only extends over three surrounding Eulerian grid points in each direction within close proximity to the Lagrangian marker. The velocity at these grid points is weighted by the Eulerian grid volume $\Delta x \times \Delta y \times \Delta z$, the product of the grid spacing along the x, y, and z directions, respectively. The velocity at the immersed boundary must then be set to the desired value by applying the necessary force, which is proportional to the difference between the desired and actual velocities on each Lagrangian marker. Finally, the

Table 2
List of Simulations

Simulation number	d_p^* (μm)	ρ_p^* (g/cm^3)	ρ_f^* (g/cm^3)	Re_p	Θ_{cr}	Θ	Θ/Θ_{cr}	Re_τ	U_τ^* (cm/s)	U_b^* (cm/s)	H_f^* (cm)	$\overline{\overline{h}}^*$ (mm)	$L_x \times L_y \times L_z$	$N_x \times N_y \times N_z$
S1	250	1.57	1.00	9.347	0.029	0.109	3.76	180	1.237	19.32	1.455	0.728	$12 \times 4 \times 1.05$	$288 \times 96 \times 301$
S2	150	1.57	1.00	4.344	0.046	0.182	4.00	180	1.237	19.32	1.455	0.728	$12 \times 4 \times 1.05$	$288 \times 96 \times 301$
S3	50	1.57	1.00	0.836	0.122	0.547	4.47	180	1.237	19.32	1.455	0.728	$12 \times 4 \times 1.05$	$288 \times 96 \times 301$
S4	250	1.57	1.00	9.347	0.029	0.055	1.88	180	0.874	13.65	2.058	1.03	$12 \times 4 \times 1.05$	$288 \times 96 \times 301$
S5	150	1.57	1.00	4.344	0.046	0.091	2.00	180	0.874	13.65	2.058	1.03	$12 \times 4 \times 1.05$	$288 \times 96 \times 301$
S6	50	1.57	1.00	0.836	0.122	0.274	2.23	180	0.874	13.65	2.058	1.03	$12 \times 4 \times 1.05$	$288 \times 96 \times 301$
$S2_f$	150	1.57	1.00	4.344	0.046	0.182	4.00	180	1.237	19.32	1.455	0.728	$12 \times 4 \times 1.05$	$432 \times 144 \times 451$
GS1	150	1.57	1.00	4.344	0.046	0.182	4.00	180	1.237	19.32	1.455	0.728	$12 \times 4 \times 1.05$	$288 \times 96 \times 301$
GS2	150	1.57	1.00	4.344	0.046	0.182	4.00	180	1.237	19.32	1.455	0.728	$12 \times 4 \times 1.05$	$288 \times 96 \times 301$
GS3	150	1.57	1.00	4.344	0.046	0.182	4.00	180	1.237	19.32	1.455	0.728	$12 \times 4 \times 1.05$	$288 \times 96 \times 301$
GS4	150	1.57	1.00	4.344	0.046	0.182	4.00	180	1.237	19.32	1.455	0.728	$12 \times 4 \times 1.05$	$288 \times 96 \times 301$
GS5	150	1.57	1.00	4.344	0.046	0.182	4.00	180	1.237	19.32	1.455	0.728	$12 \times 4 \times 1.05$	$288 \times 96 \times 301$
GS6	50	1.57	1.00	0.836	0.046	0.547	4.47	180	1.237	19.32	1.455	0.728	$12 \times 4 \times 1.05$	$288 \times 96 \times 301$
GS7	150	1.57	1.00	4.344	0.122	0.091	2.00	180	0.874	13.65	2.058	1.03	$12 \times 4 \times 1.05$	$288 \times 96 \times 301$

force on each Lagrangian marker is spread onto the surrounding Eulerian mesh using a discrete delta function. Here again, the weight of each Lagrangian marker is given by the local volume $\Delta x \times \Delta y \times \Delta z$.

The details of the first set of numerical simulations (cases S1–S6) and the physical parameters they correspond to will be further elaborated in section 4.1. Here we briefly address the adequacy of the grid in resolving bedform features and capturing the spatio-temporal evolution of the bed. To that end, we compared certain features from cases S2 and $S2_f$ in Table 2. Note that both cases are identical in terms of the physical parameters they represent, the only difference is in the grid resolution where for case $S2_f$, the grid is 50% finer than for case S2. Because of the turbulent nature of the flow, the simulations may only be compared in a statistical sense. We observe the same exponential growth rate of the incipient bedforms at early times in both simulations, and we find the wave number spectra of the bedforms to be nearly identical as well. Additionally, we find that the early stages of bed evolution, in terms of observed features (longitudinal and quasi-streamwise streaks, chevron features, incipient crestline, etc.) as well as the time sequence of development, are unaffected by the increased resolution. Further evidence on the adequacy of the grid resolution in terms of velocity spectra will be provided in section 4.2. We therefore conclude that the results discussed in this paper are not affected by the grid resolution.

IBM ensures the coupling between the flow and the bed, represented here as an internal interface. The process of evolving the bed and the back coupling from the bed to the flow occur as follows. First, we define the bed location $z = h(x, y, t)$ (see inset of Figure 1), where $h(x, y, t)$ is the time-dependent bed height with respect to the mean bed height $\overline{\overline{h}}$. Here we choose $\overline{\overline{h}} = 0.05$, which allows sufficient amount of erodible sediment in the bed as h becomes locally negative. For all cases considered in Table 2, the area of the bed that becomes dry/non erodible is less than 1.8% of the total bed area at any given time. Once the bed location is defined, we compute the shear stress from the flow field as $\boldsymbol{\tau}^* = \mu^* \nabla^* \boldsymbol{u}_t^* \cdot \boldsymbol{n}$, where $\boldsymbol{n}$ is the unit normal vector to the bed and $\boldsymbol{u}_t^*$ is the velocity vector tangent to the bed. We nondimensionalize the shear stress to obtain the local Shields number $\Theta(x, y, t)$ defined as

$$\Theta = \frac{\boldsymbol{\tau}^*}{\left(\rho_p^* - \rho_f^*\right) g^* d_p^*}. \tag{5}$$

In (5), ρ_p^* and ρ_f^* are the sediment and fluid densities, respectively; g^* is the gravitational acceleration; and d_p^* is the sediment grain diameter. We then assume the sediment volumetric flux $\boldsymbol{q}$ to be in local equilibrium with the local shear stress (Jerolmack & Mohrig, 2005) and use the modified Meyer-Peter and Müller (1948) bedload relation of Wong and Parker (2006) defined as

$$\boldsymbol{q} = \frac{\mathrm{Re}_p}{\mathrm{Re}_\tau} 4.93 \, \Theta_{cr}^{1.6} \left(\frac{\Theta}{\Theta_{cr}} - 1 \right)^{1.6} \mathbf{e}_\Theta. \tag{6}$$

where $\mathbf{e}_\Theta$ is a unit vector in the x-y plane pointing in the direction of the bed shear stress, Re_p is the sediment Reynolds number defined as

$$\mathrm{Re}_p = \frac{1}{\nu^*} \sqrt{\frac{\rho_p^* - \rho_f^*}{\rho_f^*} g^* d_p^{*3}}, \tag{7}$$

and Θ_{cr} corresponds to the value of the critical Shields number needed for sediment incipient motion (Shields, 1936). The Θ_{cr} is expressed as a function of the sediment Reynolds number Re_p as (Garcia, 2008)

$$\Theta_{cr} = \frac{1}{2}\left[0.22\ \mathrm{Re}_p^{-0.6} + 0.06\ \exp\left(-17.77\ \mathrm{Re}_p^{-0.6}\right)\right]. \quad (8)$$

The sediment bed height is then updated by solving (3), and the flow field is advanced in time taking into account the position of the newly evolved bed. The updated flow field then imposes a new shear stress on the bed and so on. The spatial derivatives in (3) are discretized using a second-order finite difference scheme, and time integration is handled using a third-order Runge-Kutta low storage scheme. Since the Exner equation as presented in (3) does not limit the streamwise or spanwise slopes of the bed, which when unconstrained can take large unphysical values, we use a mass conservative sand-slide algorithm (Sotiropoulos & Khosronejad, 2016) to limit the bed slope to the angle of repose taken here to be $\alpha_R = 30°$ (Charru et al., 2016; Coleman & Melville, 1996).

In the present study we are interested in the flow regime where the only mode of sediment migration is through bedload transport. For the sediment and flow properties under consideration the shear stress at the bed is such that the sediment migrates along the bed without being carried into the flow as suspended sediment. We are primarily interested in the formation and development of ripples in fluvial flows, where bedload transport has been deemed to be an important mechanism (Paarlberg et al., 2009). The fluvial bedforms we are interested in modeling are those with an asymmetrical triangular shape consisting of a gentle slope on the stoss side and a steeper slope (corresponding to the angle of repose) on the lee side. Engelund (1970), among others, showed that suspended sediment transport is especially important in supercritical flow regimes with Froude numbers close to or exceeding 1. In our simulations, the Froude number ranged from 0.3 to 0.5. Additionally, by limiting the Reynolds number to relatively low values, we consider the regime where suspended sediment load can be ignored.

It should be pointed out that our coarse-grained approach is at the mesoscale both for the flow and for the sediment. Since the Reynolds number of the turbulence is modest, we resolve all the scales of the flow at the mesoscale. However, there are flow scales of the order of a sediment size and these microscale flow details (or pseudo turbulence) are not resolved. Similarly, the simulations do not resolve each and every sediment grain, since each grid cell on the bed contains a large number of sediment grains. The collective motion of the particles at the mesoscale is modeled with the MPM model. The choice of MPM was motivated by the observation by Kidanemariam and Uhlmann (2017) that their fully resolved simulations was adequately captured by the model. But the results to be presented below can be reproduced with other similar bedload transport models. An alternate approach is to use Euler-Lagrange framework to simulate the motion of individual grains (Nabi et al., 2013), which in the present case are much smaller than the grid.

3. Turbulent Flow Over a Wavy Bed: A Validation Case

The present code has been utilized in the context of turbulent turbidity currents in a channel (e.g., Cantero et al., 2009) and density-driven flows (e.g., Zgheib et al., 2015a, 2015b). More recently the IBM in this code has been extensively tested and used in the context of flow over isolated particles and through a random array of spherical particles (e.g., Akiki, Jackson, et al., 2016, 2017; Akiki, Moore, et al., 2017). In the following, we will provide an additional validation of the code by considering the case of a turbulent open channel flow over a fixed wavy bed. The benchmark case considered is that corresponding to the simulation of De Angelis et al. (1997).

The numerical setup of De Angelis et al. (1997) consisted of a turbulent open channel flow at $Re_\tau \approx 171$ in a rectangular domain with periodic lateral boundary conditions. The domain size was $(2\pi \times \pi \times 1)$ with a corresponding fully resolved grid along the streamwise, spanwise, and vertical directions, respectively. The bottom wall was composed of sinusoidal waves with no lateral variation, whereas the top surface was held flat. The fixed sinusoidal waves had an amplitude-to-wavelength ratio of 0.025. No slip and no penetration conditions were enforced on the wavy wall at the bottom. Free slip and no penetration conditions were enforced on the flat surface at the top. While the same shear Reynolds number, boundary conditions, and domain size were used in the validation simulation, we have kept the grid resolution (per unit length) identical to that for the simulations in Table 2. The flow for our simulation has been averaged over 30 nondimensional time units. The results of the comparison are shown in Figure 2 for the mean streamwise component of velocity (Figure 2a), the rms velocity fluctuations (Figure 2b), and the bed shear stress (Figure 2c). We observe good agreement with the simulations of De Angelis et al. (1997). These

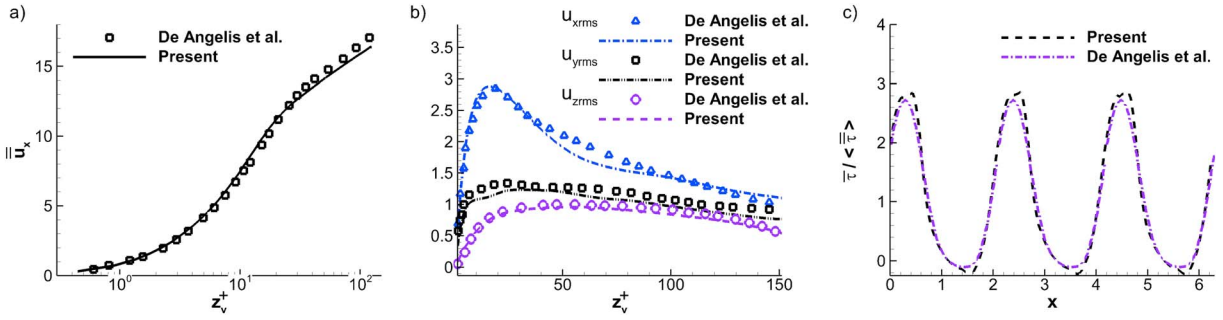

Figure 2. (a) Mean streamwise velocity profile. (b) rms of velocity fluctuations. (c) Bed shear stress.

results along with the validations provided in Akiki and Balachandar (2016), Akiki, Moore, et al. (2017) provide support for the use of the present immersed boundary methodology for resolving the turbulent flow over a rippled bed.

4. Coupled Flow-Bed Simulations

4.1. Temporal Evolution of Bedforms

It is well established that a flat sediment bed lying below a turbulent unidirectional flow is unstable and generates a wide variety of bedform structures, which depend on flow conditions and sediment properties (Coleman & Melville, 1996; Kennedy, 1969; Nielsen, 1981; Nelson & Smith, 1989). For Froude numbers typically less than about 0.5 to 0.7, downstream migrating bed waves develop, these are termed ripples or dunes depending on their size, behavior, and sedimentary origin (grain size, shear stress, etc) (Engelund & Fredsoe, 1982; McLean, 1990; Richards, 1980), while at higher Froude numbers, upstream traveling bed waves known as anitdunes may form. In this paper, we are solely concerned with the temporal evolution of ripple-like structures from an initially flattened bed. The initial evolution and development of ripples have been well documented in the earlier experiments of Baas (1994), Venditti et al. (2005), and more recently by Perillo, Best, et al. (2014). Additionally, using numerical simulations, Sotiropoulos and Khosronejad (2016) have shown that they are able to reproduce certain aspects of ripple formation at early stages. Here we show using coupled, flow-bed simulations that we are able to capture the various stages of ripple formation observed in experimental flumes, namely, (i) the initial longitudinal streaks, (ii) the chevron features, (iii) the incipient crestlines, and (iv) the straight/sinuous ripples. However, we do not observe the equilibrium linguoid ripples (3D bedforms) that evolve from the straight/sinuous ripples due to the secondary instability of the crestlines along the spanwise direction. We note that the spanwise extent of the computational domain is chosen to be 4 times the flow depth (see Table 2), which likely limits large-amplitude spanwise deformation and the formation of stable equilibrium linguoid ripples over long time scales. Moreover, the periodic nature of the boundary conditions applied along the span as opposed to applying a smooth wall condition may additionally affect the transition to 3D bedforms. For example, Nabi et al. (2013) simulated 3D dunes that resulted from 2D straight dunes with smooth sidewall boundary conditions. Even though this transformation from the straight/sinuous ripples to the linguoid ripples is well documented in nature, it has been shown to be dependent on the nature of the numerical model, especially the lateral boundary condition. For example, perhaps due to periodic lateral boundary condition, sinuous ripples were absent even in the fully resolved direct numerical simulations (Kidanemariam & Uhlmann, 2017). Jerolmack and Mohrig (2005), for instance, were able to generate 3D bedforms by adding a low-amplitude noise as a source term in the Exner equation (3).

The first six simulations in Table 2, S1 through S6, evolve from an initially flattened bed. Before the start of each simulation, the bed is kept flat, and the flow is allowed to reach a stationary turbulent state. Then, the bed is allowed to evolve according to the Exner equation (3) starting at $t = 0$. These simulations are the focus of the present section (section 3). For these cases, as well as all the others in Table 2, the friction Reynolds number has been fixed at $Re_\tau = 180$. Even though the bulk of the analysis is done using nondimensional parameters, we will briefly discuss here the corresponding physical parameters of each of these simulations. To arrive at those physical parameters, we first choose the sediment and fluid properties as shown in

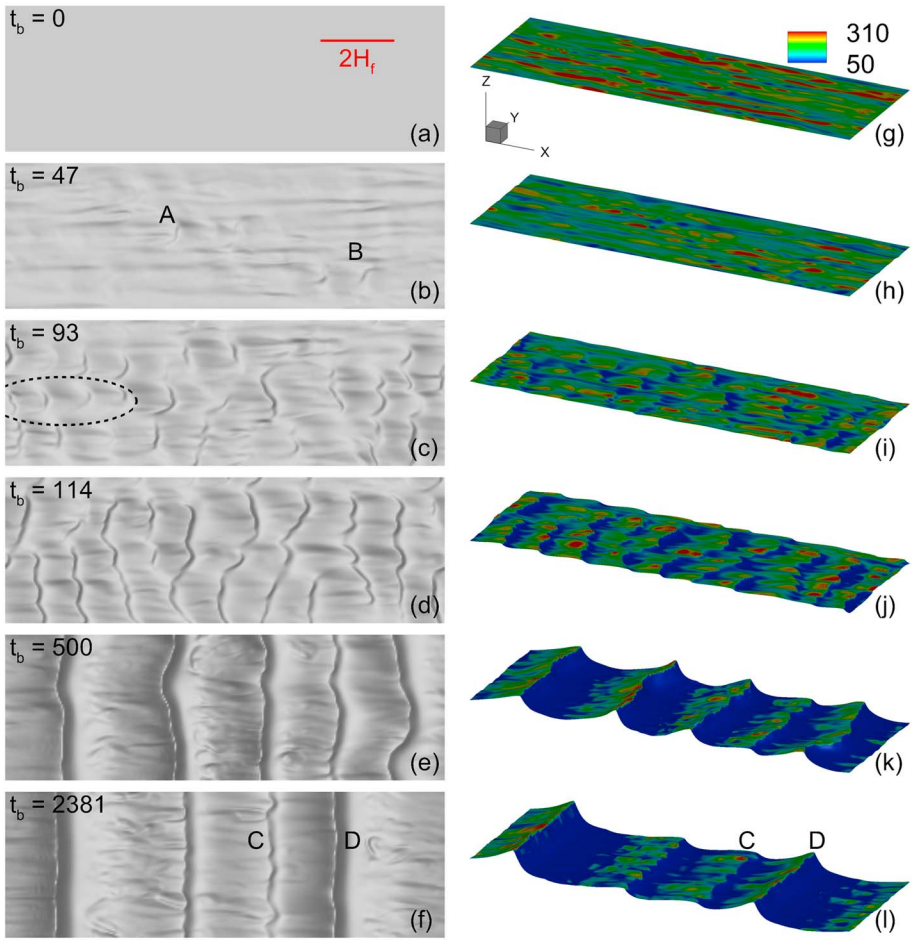

Figure 3. Top (left) and isometric (right) views of the temporal evolution of the bed from S2. The vertical z coordinate is stretched by a factor of 4 for clarity. Flow is from left to right. The contours in the isometric view correspond to the bed-normal tangential velocity gradient $\partial u_{tx}/\partial n$. The marks A and B in frame (b) correspond to cross-stream streaks. The dashed ellipse in frame c encloses a train of chevron features. The red segment in the upper right corner of frame a shows the scale of the bedforms. It is twice the length of the mean fluid depth.

Table 2, and then decide on a value for the Shields number Θ. We can then solve for the shear velocity and flow depth, since Re_τ is fixed.

First, from these six cases, we distinguish two sets. The first set is for a relatively higher bed shear velocity value of $U_\tau^* = 1.237$ cm/s (cases S1, S2, and S3) ,whereas the second set (cases S4, S5, and S6) is for a relatively lower bed shear velocity of $U_\tau^* = 0.874$ cm/s. Since the working fluid, water, is the same in all cases, and Re_τ is fixed, it follows then that the flow depth for cases S1, S2, and S3 must be shallower ($H_f^* = 1.455$ cm) than that for cases S4, S5, and S6 ($H_f^* = 2.058$ cm). In each of these two sets, the sediment has the same grain density ($\rho_p^* = 1.57$ g/cm^3), chosen to match the experiments of Fedele et al. (2014, 2016), but three different grain sizes, namely, $d_p^* = 50, 150,$and 250 μm, for which the sediment Reynolds number remains confined to values less than 10. Figure 3 shows a top three-dimensional view (left) and an isometric view (right) of the evolving bed at six different time instances. These images correspond to case S2. In the top view, lighting effect is used that highlight regions with a sharp elevation gradient. That is, in frames c to f, the darker transverse lines correspond to a relatively sharp drop in the bed elevation along the streamwise direction, and thus are well suited to capture the location of key bedforms such as crestlines and ripples. Also shown on the right frames are iso-contours of the bed-normal gradient of tangential velocity $\partial u_{tx}/\partial n$ plotted on the bed. Here u_{tx} is the magnitude of the tangential velocity with respect to the bed along the streamwise direction and t_b is the nondimensional bulk time, defined as $t_b = t^* U_b^*/H_f^*$. Here U_b^* corresponds to the bulk velocity at the start of the simulation

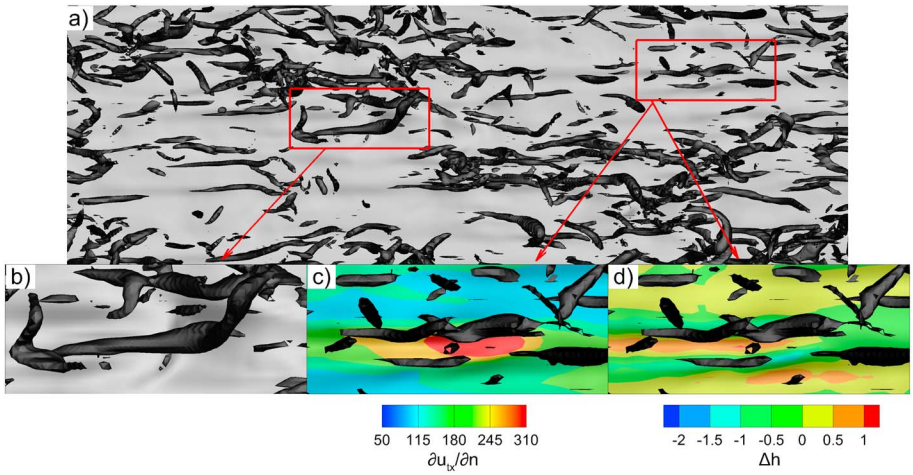

Figure 4. Top view of the bed from S2 at t_b = 47 (same as in Figure 3e). (a) Iso-surfaces of λ_{ci} = 20 over the entire bed. (b) Enlarged view showing a cane-shaped vortex near the cross-stream streak *A* in Figure 3e. (c) Enlarged view showing the near bed low-speed and high-speed streaks from iso-contours of the bed-normal tangential velocity gradient $\partial u_{tx}/\partial n$. (d) Same as frame c but with iso-contours of the Laplacian of *h* showing longitudinal streaks with high and low bed elevation.

$$U_b^* = \frac{1}{H_f^* L_y^*} \int_0^{H_f^*} \int_0^{L_y^*} u^* \, dy^* \, dz^* \approx 15.6 U_\tau^*. \tag{9}$$

At t_b = 0, at the start of the simulation, the flow corresponds to a fully developed, Re_τ = 180 turbulent open channel flow over a flat bed. At t_b = 47, longitudinal streaks are easily discerned. These are aligned predominantly with the flow direction with only a few aligned at an angle to the flow. These sediment streaks are the imprints of the quasi-streamwise vortices and hairpin vortex packets (see Figure 4) that travel downstream (Zhou et al., 1996, 1999). Iso-surfaces in Figure 4 correspond to the swirling strength λ_{ci}, which is defined as the absolute value of the imaginary portion of the complex eigenvalue of the velocity gradient tensor. The λ_{ci} provides a good metric for identifying regions of intense vortical structures (Chakraborty et al., 2005; Zhou et al., 1999) such as inclined quasi-streamwise hairpin and horseshoe-shaped vortical structures, which span the entire planform of the bed. The enhanced shear stress on the bed under these quasi-streamwise vortices rearranges the bed along the spanwise direction. It has been established that due to the autogeneration mechanism, these near-bed vortical structures are aligned along the streamwise direction, with each subsequent vortex reinforcing the influence of its streamwise predecessors. This results in the formation of longitudinal streaks of high and low bed elevation (see Figure 4). This mechanism is identical to the formation of near-wall low-speed streaks in turbulent boundary layers (Adrian et al., 2001). Thus, we observe the longitudinal streaks of higher bed height to be well correlated with local regions of low streamwise velocity (Figure 4). The streaks are highly correlated in the streamwise direction such that they can be several flow depths in length, but only about one sediment grain diameter in height.

The near-wall region of a turbulent boundary layer is also populated with hairpin and cane-shaped (which are one-sided hairpin) vortices (Chakraborty et al., 2005; Zhou et al., 1999), whose heads are spanwise oriented. Movies of the time-evolution of the bed with superposed vortex structures suggest that occasional intense hairpin vortices are responsible for the incipient bedforms that are oriented at an angle to the streamwise direction (marked A and B in Figure 3b). These incipient cross-stream bedforms quickly develop into chevron-shaped features, which initially form at random locations in the bed where there are intense vortex structures. Once formed, these chevron shapes straighten and spawn new incipient cross-stream bedforms along the downstream direction at a preferred wavelength of about 1.2 nondimensional units. Several such trains (Coleman et al., 2003) of incipient cross-stream bedforms are seen at t_b = 93 (Figure 3c). Although the mechanism leading to the formation of these chevron trains is still not fully understood, in section 5 we will explore the tendency for an incipient cross-stream bedform to form a train of self-similar structures. The mechanism of bed formation at the very early stages is difficult to analyze, especially in experiments, due to the very rapid growth of these bedforms and their quick evolution to fully formed ripples (Perillo, Prokocki, et al., 2014). These chevron features have very small amplitudes of approximately one sediment

grain size. We should note, however, that hairpin vortices do not represent the only mechanism for inducing incipient bedforms, as they do form even under laminar flow conditions.

The chevron features grow laterally and merge to form more developed crestlines at $t_b = 114$ (Figure 3d). The process by which this lateral expansion occurs is discussed in section 4.3.1. These crestlines are still of low amplitude at about 1 to 2 sediment grain diameters. Both chevron and incipient crestlines cover the entire bed and seem to exhibit a somewhat regular spacing in the streamwise direction (Coleman & Melville, 1996) of about 1.2 to 1.5 nondimensional units (flow depth). The crestlines are predominantly aligned with the cross-flow direction and display a rather wavy pattern (2.5D; Perillo et al., 2014). The incipient crestlines grow in amplitude to form straight/sinuous ripples at $t_b = 500$. These ripples continue to grow and develop (and are hence termed developing ripples). The developing ripples possess a well-defined triangular cross-sectional shape with a gentle slope on the stoss side and a steeper lee side. For large enough ripples, flow separation occurs downstream of the ripple and is characterized by low bed shear stress values on the lee side (see frames k and l in Figure 3).

At any instance during the bed development, the size of the ripples is quite different (see for example frames k and l). Since, smaller bedforms move faster than larger ones (Coleman & Melville, 1994; Hino, 1968; Kennedy, 1969), coarsening occurs (e.g., Andreotti & Claudin, 2013) as upstream smaller and faster ripples interact with the downstream larger and slower moving ripples. For example, the bed seen in frames e and k contains five prominent ripples of varying elevation. As they evolve over time the bedforms coarsen to have only four dominant ripples in frames f and l. Even here we can clearly observe the third ripple from the left (marked C) to be much smaller (in height) than the others, and as a result it travels faster. When allowed to evolve further the bedform continues to coarsen to have only three ripples. However, the process by which the bed evolves to three ripples occurs as follows: As the smaller third ripple (C) continues to approach the larger fourth ripple (marked D), it ends up starving the larger one, which eventually dies, and the initially smaller third ripple grows into a bigger ripple. We discuss this bedform interaction process further in section 4.3. However, it should be noted that the time taken for coarsening from four to three ripples is much longer than the time taken for coarsening from five to four ripples. The bedform interactions leading to coarsening as well as the rate of coarsening will be addressed in greater detail in Paper 2.

It should be noted that the near-bed turbulent structures such as low-speed streaks and hairpin vortices are streamwise oriented, and they are predominantly aligned along the streamwise directions to form packets (Zhou et al., 1999); nevertheless, the dominant bedforms (ripples and crestlines) are spanwise oriented. Starting from a flat bed, the bedforms that initially emerged are indeed streamwise oriented, but very quickly, self-organization of the bed naturally leads to spanwise oriented structures that are quasiperiodic along the streamwise direction. In a laminar flow, it is well recognized that spanwise oriented ripples naturally form due to an instability that arises from the phase shift between a sinusoidal perturbation to the bed height and the shear stress on the bed. Stability analysis performed on turbulent mean flow also explains the formation of spanwise ripples (Coleman & Fenton, 2000; Colombini, 2004; Engelund, 1970). Nevertheless, the imprint of self-organization and emergence of coherent spanwise bedforms in a fully turbulent flow can be recognized. Underlying local mechanisms of interaction between the turbulent flow structures and the sediment that were observed early on in Figure 3b are still present at later times. For example, in frames e and f of Figure 3, the effect of quasi-streamwise vortices can be clearly seen on the stoss side as streamwise streaks in bed height. We can also observe local sediment piles generated by the heads of hairpin and cane-shaped near-bed vortex structures. As the vortex structures propagate forward along the stoss side, relative to the ripple, these small sediment piles also get pushed along toward the crest of the ripple. This is an important mechanism by which sediment gets transported along the stoss side and contributes to the building of the ripple. Thus, the constant interaction between the flow and the bed contributes to the self-organization and growth of the bedform.

Morphodynamic systems are defined by the coupling between flow, sediment transport, and bed morphology. Spatial and temporal changes in flow conditions, sediment transport through linear and nonlinear mechanisms, and large- and small-scale changes in bed topography are driven by the intertwined processes of fluid dynamics, sediment transport, and bed morphology (Best, 1993; Leeder, 1983; Perillo, 2013). Bedforms, such as ripples, change the details of the near-bed turbulent flow; for example, flow separation on the lee side alters the interaction between quasi-streamwise vortical structures and the bed. This can

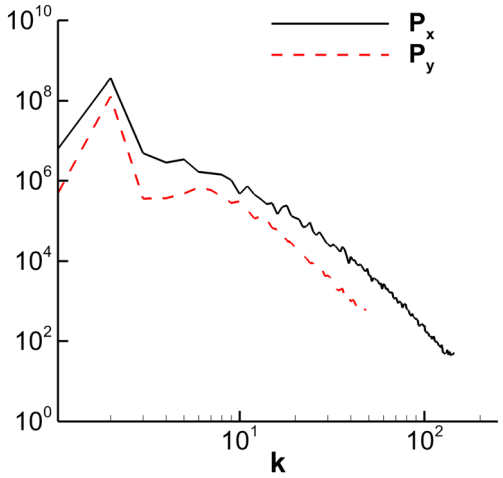

Figure 5. Spanwise-averaged x-energy spectra P_x and streamwise-averaged y-energy spectra P_y of the streamwise component of velocity at $z = 0.15$ at a time instance where the tallest ripple has grown to a height of $z = 0.14$.

be clearly observed as the lower values of shear-stress along the bed downstream of the first ripple and the fourth ripple marked D in Figure 3l. Each bedform has the power to alter the interaction between the flow and the bed on its downstream side, which will in turn affect the generation, growth, or destruction of downstream bedforms. Thus, the interaction between bedforms, flow structures, and sediment transport is coupled in a complex way.

4.2. Flow Field Dynamics

Bedform evolution is primarily governed by the coupling between the bed and the flow. It is the flow in the vicinity of the bed that dictates the bottom shear stress and hence strongly influences the development of bedforms. In return, near-bed turbulence is most affected by bed topology and the resulting back coupling to the flow. It is this strong coupling between bed and flow that is essential for furthering our understanding of the various mechanisms of bed formation. Experimental studies (Baas, 1994; Coleman & Melville, 1996; Coleman et al., 2003; Fedele & García, 2009; Kennedy, 1969; Nelson & Smith, 1989; Perillo, Best, et al., 2014; Perillo, Prokocki, et al., 2014; Venditti et al., 2005) have illuminated aspects of short and long time evolution of the bed morphology. However, it has been difficult to establish the connection between individual turbulent flow structures and their effect on the formation and evolution of the ripples. The difficulty is due to the complexity of measuring the turbulent flow above a mobile deforming bed in such small-scale detail. First we show in Figure 5 spanwise-averaged x-spectra and streamwise-averaged y-spectra of the streamwise velocity component at $z = 0.15$ for case S2 at a time instance where the tallest ripple has grown to $z = 0.14$. Thus, the elevation is just above the tallest ripple and passes through a horizontal plane that includes intense vortical structures. Both spectra show more than six orders of decay in magnitude indicating adequate resolution along both the streamwise and spanwise directions. Similar investigation along the bed-normal direction shows adequate spectral decay as well.

Let us start by inspecting the flow field to better visualize the coupling between the bed and the flow and to detect regions of flow reversal. Figure 6 shows iso-contours of the spanwise-averaged streamwise component of velocity above the nearly span invariant ripples from case S2 at $t_b = 1500$. The components of the velocity vectors in the main figure and the inset are the span-averaged $\overline{u}_x$ and $\overline{u}_z$ along the x and z directions, respectively. Spanwise averaging, for example, in the case of $\overline{u}_x$, is performed as follows

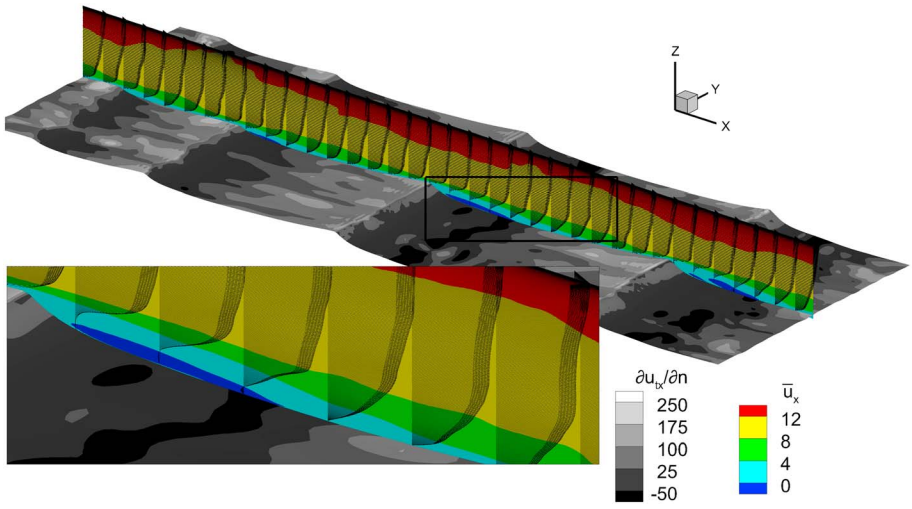

Figure 6. Isometric view of the bed from S2 at $t_b = 1500$. The gray scale contours on the bed correspond to $\partial u_{tx}/\partial n$, and the contours in the center plane correspond to $\overline{u}_x$. The components of the vector field are $\overline{u}_x$ and $\overline{u}_z$. The inset shows an enlarged view where the region of separation and flow reversal downstream of the ripple is marked by the dark blue color (negative $\overline{u}_x$ values).

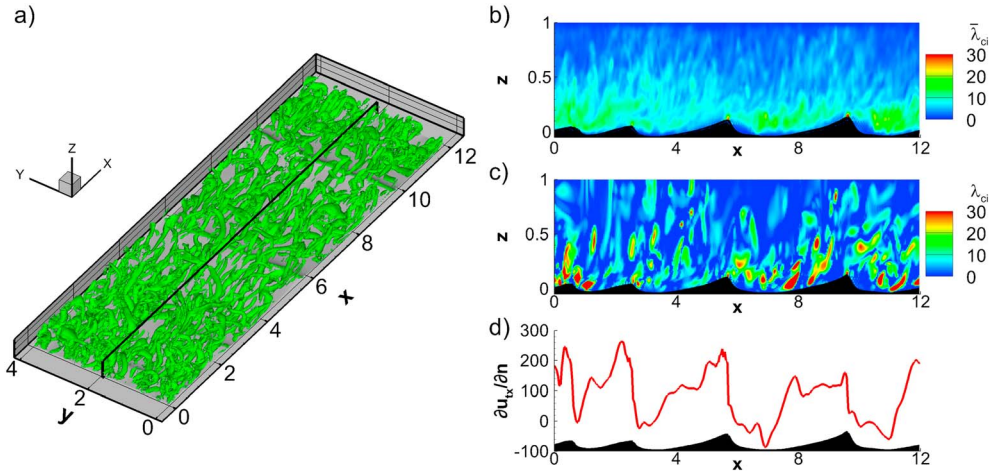

Figure 7. Data corresponding to case S2 at t_b = 1500. (a) Iso-surfaces of λ_{ci} = 15. (b) Iso-contours of $\overline{\lambda}_{ci}$ over the span-averaged bed height $\overline{h}$. (c) Iso-contours of λ_{ci} in the y = 2 plane. (d) Local streamwise variation of the x component of the bed-normal gradient of tangential velocity, $\partial u_{tx}/\partial n$ in the y = 2 plane.

$$\overline{u}_x\,(x,z,t) = \frac{1}{L_y}\int_0^{L_y} u_x dy. \tag{10}$$

The inset in the figure shows an enlarged view of the averaged flow field downstream of the ripple. Flow reversal (negative $\overline{u}_x$ values) is indicated by a dark blue color, and the separation bubble extends downward toward the bed below the "green" shear layer region. The vertical gradient of streamwise velocity $(\partial\overline{u}_x/\partial z)$ is observed to progressively steepen beyond the recirculation region (see inset of Figure 6). This provides an indication of flow reattachment and boundary layer redevelopment downstream of the separation region. Here, and in the remainder of this paper, an overbar denotes spanwise averaging.

The flow displays strong variation in the spanwise direction as evident from the grey scale iso-contours of the bed-normal gradient of tangential velocity $\partial u_{tx}/\partial n$. The near bed flow is strongly correlated, as expected, with the bed shear stress. Indeed, we observe flow separation to result in negative values of $\partial u_{tx}/\partial n$ (black iso-contour) downstream of the crest, whereas we observe $\partial u_{tx}/\partial n$ to attain its largest values (light grey iso-contours) on the stoss side of the ripples.

The turbulent flow structure above the bed is far more complex as can be seen from the iso-contours of the swirling strength in Figure 7a. Figure 7 corresponds to case S2 at t_b = 1,500. Because of the no-stress boundary condition at the free surface (top boundary of the computational domain), vorticity is only generated on the bed and is transported upward by turbulent diffusion. However, regions of strong vortical structures only marginally penetrate beyond the upper half of the channel. We observe from Figure 7b that $\overline{\lambda}_{ci}$ remains relatively small within a very thin layer just above the bed. We distinguish regions of low turbulence intensity downstream of the developing ripples and below the shear layer induced by flow separation (Best, 2005; Müller & Gyr, 1986). Indeed, depending on the size of the ripple, flow separation may occur on the lee side (note the two blue regions downstream of the ripples around $x \approx 6$ and 10), which results in local turbulence suppression. The flow therefore imposes on the bed a low, nonerosive, shear stress in the separation region before bedload transport is resumed farther downstream when the flow reattaches to the bed. This explains the low values of $\overline{\lambda}_{ci}$ in the recirculation region downstream of the ripple. The presence of these recirculation regions results in a nonuniform streamwise distribution of $\overline{\lambda}_{ci}$ near the bed within a depth equivalent to the height of the ripples. Finally, we observe the low turbulence, separation region to extend beyond the crest to about 3 times the ripple height on average. We will discuss flow separation in more detail in Paper 2.

Since at later times, the bed topology is nearly span-invariant, a vertical slice of the instantaneous swirling strength provides a good means for visualizing the turbulence intensity in the flow field, close to as well as far away from the bed. Figure 7c corresponds to a vertical cross section of the domain at $y = L_y/2$ showing iso-contours of λ_{ci} over the local bed elevation. We observe the flow to be very complex, with multiple

vortical structures at close proximity to the bed. Unlike its span-averaged counterpart, here λ_{ci} may locally attain larger values (yellow and red regions) and exhibit much stronger spatial variations. If we consider, for example, the region extending between $x \approx 6$ and $x \approx 8$, that is the region downstream of the third ripple, we observe multiple strong vortex cores, which correspond to a streamwise train of hairpin-like vortex structures. The distance between these vortices and the bed decreases the farther out they extend from the crest along the streamwise direction. This is consistent with flow separation and reattachment downstream of the lee side. Thus, although turbulent vortex structures are seen to be present nearly evenly in the *x-y* plane, they are separated (or detached) from the bed on the lee side of the dominant ripples. This alters the flow-induced sediment transport process on the stoss side of the downstream ripple.

The imprint of the turbulent flow field on the bed is manifested as a turbulent bed shear stress profile at the sediment interface. Figure 7d shows the local streamwise variation of the *x* component of the bed-normal gradient of tangential velocity, $\partial u_{tx}/\partial n$, on the erodible bed (shown in black) in the center plane $y = 2$. The bed exhibits large variations in $\partial u_{tx}/\partial n$ with the local maxima occurring on the stoss side of the ripples, just upstream of the crests. On the other hand, local minima, which correspond to flow reversal, occur downstream of the crest. The magnitude of the flow reversal and the region over which flow reversal occurs are strongly dependent on the ripple height. Larger ripples form bigger separation bubbles with higher reverse flow magnitudes. Consequently, because the maxima and minima occur just upstream and downstream of the crests, respectively, we observe the largest jump in values of $\partial u_{tx}/\partial n$ to occur in the vicinity of the crest.

4.3. Bedform Interactions

A rich spectrum of bedform interactions occurred during the development of the bed in the simulations. These interactions have been observed in aeolian and subaqueous bedforms (Kocurek et al., 2010) and constitute an essential mechanism for the self-organization process of bedforms. Kocurek et al. (2010) provide a thorough summary of the various interactions documented in laboratory experiments as well as field studies (Ewing & Kocurek, 2010; Elbelrhiti, Andreotti, & Claudin, 2008; Endo et al., 2004; Hersen & Douady, 2005; Hersen et al., 2004; Kocurek et al., 1992; Sharp, 1963). They classified some of these interactions as constructive, for example, lateral linking and merging, which result in fewer, larger, and more widely spaced bedforms, or regenerative such as bedform splitting and defect creation, which result in smaller bedform features. Other interactions like bedform and defect repulsion as well as remote interactions do not fall under the above two categories, but rather lead to bedform rearrangement through a pattern change. In our simulations, we observe many such documented interactions including lateral linking, defect and bedform repulsion, defect creation, remote interactions, and merging. These interactions, which provide simplified insights to bedform self-organization in more complicated natural systems, are present in all our simulations. In the interest of brevity, we will show a few examples as we attempt to shed some light on the mechanisms behind these interactions.

4.3.1. Lateral Linking

To help illustrate a time sequence for lateral linking (e.g., Kocurek & Ewing, 2005; Landry & Werner, 1994; Werner, 1995) between two incipient crestlines, we show in Figure 8 a top view of the bed for case S3 at three time instances, namely, $t_b = 94$, 98, and 112 corresponding to frames a, b, and c, respectively. These frames illustrate that the sequence is denoted by a pair of inclined, upward, and downward facing arrows in frames a_1, b_1, and c. For the purpose of clarity, bedform features are exaggerated by stretching the vertical *z* direction by a factor of 4. This stretching is in fact done for all the figures in section 4.3 that display the three-dimensional top view. Lateral linking constitutes a constructive interaction in aeolian and subaqueous bedforms and helps to decrease bed defect density. It is a dominant process in the early stages of bed evolution, but may also occur between smaller defects riding on the stoss sides of larger structures (e.g., Kocurek et al., 2010). Lateral linking appears to be a continuous and smooth process in which bedforms continually grow or expand laterally, and this process of spanwise growth eventually leads to their linkage. However, by looking at multiple snapshots of the process with iso-contours of the instantaneous volumetric flux of sediment *q*, we observe the lateral expansion to occur in bursts. Indeed, if we consider frame a_1 where we show iso-contours of q_y, the instantaneous *y* component of the sediment flux, we observe the region on the stoss side of the laterally expanding crestlines to locally exhibit strong spanwise fluxes. When patches of high streamwise velocity approach the stoss side of the incipient crestlines, the flow must negotiate its way around the bedform, and part of the relatively high velocity fluid goes around the crest toward the region with lower bed elevation. This is apparent in frame a_2, which is an enlarged view of the dashed rectangle in frame a_1. Here

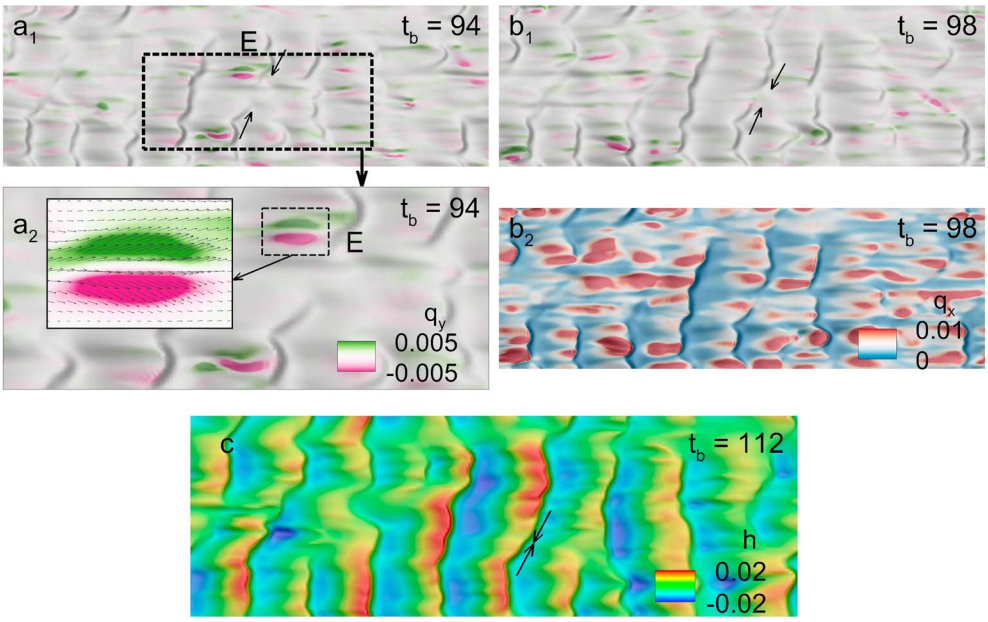

Figure 8. Lateral linking from S3. (a_1) Top three-dimensional view with iso-contours of the instantaneous spanwise flux q_y. The inclined arrows indicate the direction along which the linking is taking place. (a_2) Enlarged view of the dashed rectangle in a_1. (inset) Two-dimensional view with a vector plot of components q_x and q_y. (b_1) Same as a_1 but for a later time when the interacting bedforms are closer to one another. (c_1) Same as b_1 but with iso-contours of q_x. (c) Top three-dimensional view with iso-contours of bed elevation at a time where the lateral linking is complete. Flow is from left to right in all frames, and the vertical z-direction is exaggerated by a factor of four.

we observe the flow to exhibit a strong spanwise component of q in both the $+y$ and $-y$ directions, denoted by the green and purple patches, respectively. In the case of the crestline marked E, the purple patch, which represents a locally negative value of q_y, will contribute to the lateral expansion toward the lower end of the frame. We should note, however, that at this specific instance ($t_b = 94$) the green patch on the lower bedform will not directly contribute to lateral linking as it is not near the defect termination. The inset in frame a_2 corresponds to a two-dimensional enlarged view of the dashed rectangle, where, in addition to the iso-contours of q_y, we show a vector plot with components q_x and q_y, along the x and y directions, respectively. In the case of the purple patch, the vector plot shows the sediment being eroded from the stoss side toward lower end of the crestline at an angle of about 30° with respect to the x axis.

In frame b_1 and b_2, the bed is shown at a later time where the gap separating the two incipient crestlines has been approximately cut in half to a distance of about 0.35 units. For frame b_1, where iso-contours of q_y are displayed, we do not observe the crestlines in question to exhibit the same strong, locally acting spanwise sediment fluxes. On the other hand, such strong spanwise fluxes are observed to act on other parts of the bed, just upstream of incipient crestlines. This is consistent with the fact that crestlines do not expand laterally in a smooth continuous manner, but rather in bursts. These episodic events by which incipient crestlines grow laterally are related to the passage of quasi-streamwise vortical structures, such as those shown in Figures 5 and 7. The time interval between these bursts can, however, be very small such that the process appears smooth and continuous. In frame b_2, we show iso-contours of q_x and note that the bed exhibits strong streamwise and spanwise variation in the sediment flux, which is indicative of the turbulent nature of the flow. Finally, by $t_b = 112$ in frame c, the crestlines have collided to form one coherent structure. From the iso-contours of h, we observe the linked region to exhibit a lower elevation than the remaining part of the newly formed crestline. A possible explanation is that the crest height at the point of contact needs some finite time to grow to the size of the laterally connecting bedforms.

4.3.2. Defect Repulsion

A time sequence, composed of three snapshots from case S3, is used to illustrate the process of defect repulsion (Anderson & McDonald, 1990; Landry & Werner, 1994) in Figure 9. The process is also known as defect migration (e.g., Werner & Kocurek, 1997, 1999). Werner and Kocurek (1997, 1999) outline

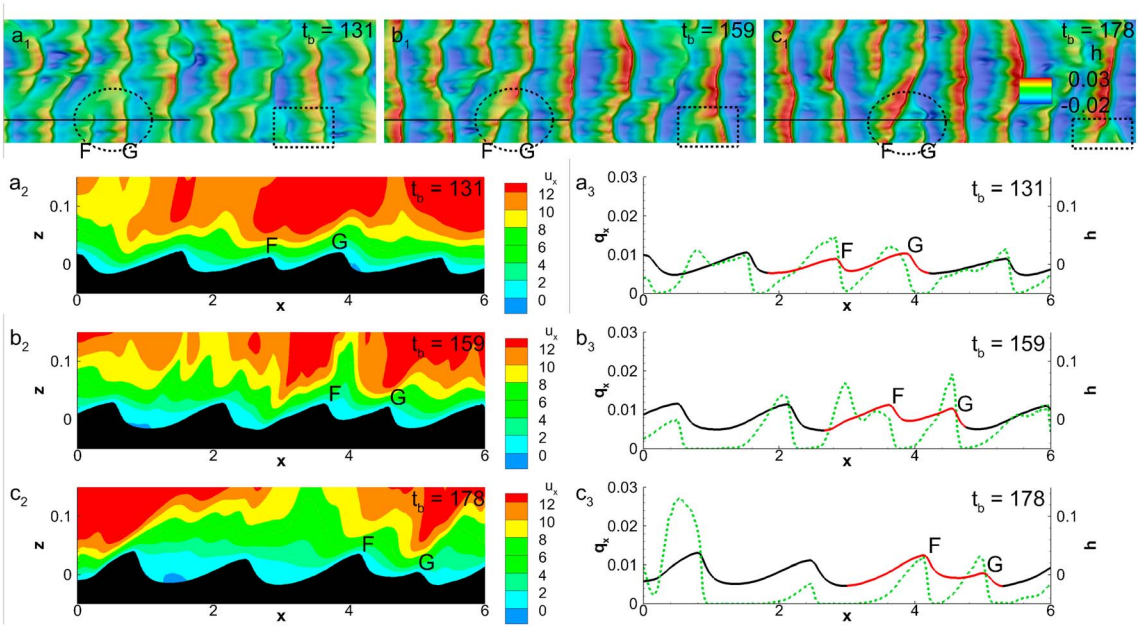

Figure 9. Defect repulsion from S3. (a_1) Top three-dimensional view with iso-contours of bed elevation showing the relative size of the interacting bedforms enclosed within the dashed ellipse. (b_1) Same as a_1 but for a later time when the defect has attached itself to the bedform and about to repel the corresponding downstream portion. (c_1) Same as a_1 and b_1 but at a later time when the repulsion is complete. In all three frames, vertical *z* direction is enlarged by a factor of 4. The dashed rectangle in a_1, b_1, and c_1 points to another defect repulsion interaction occurring at the same time. (a_2, b_2, and c_2) Cross-sectional view corresponding to the *y* position and size of the solid black segment in a_1 with iso-contours of u_x. (a_3, b_3, and c_3) Streamwise variation of *x* component of flux q_x (dashed green line) and *h* (solid black line with red highlights) along the corresponding black segment in a_1. The red portion of the bed corresponds to the interacting bedforms enclosed within the dashed ellipse of the top view frames. Flow is from left to right.

conceptually how these defect migration interactions control the pace and style of many bedform processes and properties. The frames a, b, and c in Figure 9 correspond to a time of t_b = 131, 159, and 178, respectively. First consider the top view of the bed in frames a_1, b_1, and c_1, in which the region where defect repulsion occurs is encircled within a dashed black ellipse. The iso-contours in these frames correspond to the bed elevation *h* and are used to help explain the different propagation speeds of the interacting bedforms. Additionally, in each of these frames, the black straight segment, which cuts through the dashed ellipse, corresponds to the spanwise location y = 0.75 at which a cross-sectional view is extracted in frames a_2, b_2, and c_2. In these frames, the bed elevation is shown along with iso-contours of the instantaneous streamwise component of velocity, u_x. The iso-contours help to identify recirculation regions of locally negative values of u_x marked in blue, and the cross-sectional view allows us to readily identify the structure of bedforms as they interact. Finally, in the last set of frames a_3, b_3, and c_3, we show the streamwise distribution of the sediment flux q_x (dashed green line) along with the bed elevation *h* (solid black line with highlighted red portions) corresponding to each of the respective frames a_2, b_2, and c_2. The highlighted red portions help to identify the bedforms that are undergoing defect repulsion.

Defect repulsion is the process by which a relatively smaller upstream defect propagates toward a relatively larger bedform downstream, attaches itself at one location, while repelling and replacing a portion of the downstream bedform. This mechanism, which allows defects to propagate in a rippled bed (Anderson & McDonald, 1990), was first simulated by Landry and Werner (1994). The process is similar to a relay race in the sense that a downstream defect may not be liberated until the bedform from which it is repelled comes into contact with the upstream defect. In fact, during early phases of bed evolution, when bedforms are relatively closely spaced in the streamwise direction, a single-defect repulsion can initiate other defect repulsions downstream. These processes occur in a sequential manner in both time and space and terminate when the defect merges with the downstream structure or is starved by the newly formed upstream bedform (as opposed to repelling yet another defect). Field observations by Ewing and Kocurek (2010) at White Sands suggest that defect repulsion is a pervasive interaction and a dominant form of pattern evolution.

Table 3
Approximate Size and Speed of Interacting Bedforms Before and After the Interaction

Interaction label	Figure number	Size (before interaction)	Speed (before interaction)	Size (after interaction)	Speed (after interaction)
Defect repulsion	9	(F) : 0.020 − (G) : 0.030	(F) : 0.029 − (G) : 0.022	(F) : 0.035 − (G) : 0.020	(F) : 0.028 − (G) : 0.036
Bedform repulsion	10	(I) : 0.040 − (J) : 0.060	(I) : 0.023 − (J) : 0.017	(I) : 0.050 − (J) : 0.045	(I) : 0.018 − (J) : 0.020
Bedform merging	11	(J) : 0.040 − (K) : 0.055	(J) : 0.016 − (K) : 0.013	(J + K) : 0.045	(J + K) : 0.0069
Defect creation	12	(L) : 0.030 − (M) : 0.015	(L) : 0.0022 − (M) : 0.0067	$(L) : 0.025 - \begin{matrix}(M_1) : 0.035 \\ (M_2) : 0.020\end{matrix}$	$(L) : 0.0069 - \begin{matrix}(M_1) : 0.0053 \\ (M_2) : 0.0069\end{matrix}$

Note. Bedform size is defined here as the vertical drop from crest to subsequent trough, and the crest speed is normalized by the initial bulk velocity.

Considering the size of the interacting bedforms from our simulations, the upstream defect marked F is initially smaller (frames a_1, a_2, and a_3) than the downstream bedform marked G and hence travels faster. However, as the crestlines of the bedforms come into contact with one another (frames b_1, b_2, and b_3), we observe the upstream defect F and the repelled portion of the bedform G to have nearly the same crest elevation. Finally, at the end of the process (frames c_1, c_2, and c_3), the initially upstream defect F is now significantly larger than the repelled bedform G. An estimate of the bedform size and speed before and after the interaction is shown in Table 3. Similar approximations are also provided for the subsequent flow-aligned interactions (bedform repulsion, bedform merging, and defect creation) in the following sections.

The third set of frames (frames a_3, b_3, and c_3) provides additional clues on how this process occurs. Even though the defect F is too small at $t_b = 131$ to have a fully formed recirculation region on its downstream side (there is no discernible region of negative streamwise velocity), it still modifies the flow. This is done in such a way that the sediment fluxes on its lee side and on the leading portion of the stoss side of the downstream bedform G are very small/nonerosional compared to the sediment flux on the remainder of the stoss side of the downstream bedform G. Moreover, as the upstream defect F travels faster, the aforementioned region with very small/nonerosional sediment flux grows to cover a larger portion of the stoss side of the downstream bedform G (frame b_3). Additionally, as the separation distance between the interacting bedforms decreases, and the height of the upstream defect F increases, it becomes more difficult for the flow to adjust as it passes beyond the crest of the upstream defect F. This results in a larger sediment flux just upstream of the crest of the soon-to-be-repelled portion of the bedform G. The soon-to-be-repelled bedform G now experiences a nonerosional flow over the first half of its stoss side (which halts the sediment supply toward its crest) and a highly erosional flow over the second half. This causes the repelled bedform G to travel faster downstream and diminish in size simultaneously (frame c_3). We should note that the aforementioned flow dynamics only occurs in the region downstream of the initial defect and does not extend laterally outward where the defect's height drops and levels off with the quasi-flat bed. This explains why the repelling and repelled bedforms have comparable widths.

The preceding observations on the amount of sediment flux on the stoss side of ripple G are based on the plot of q_x presented in frames a_3, b_3 and c_3 of Figure 9. Some care is required in interpreting these plots. Note that from (3), it is the divergence of q that contributes to $\partial h/\partial t$, ignoring the effect of diffusion. Here again the effect of the ripple's downstream advection must be separated to infer its temporal growth or decay. A one-dimensional bedform that simply advects along the streamwise direction at uniform velocity U is given by $h(x,t) = f(x - Ut)$, and it can be readily seen that the corresponding streamwise sediment flux will be given by

$$q(x,t) = \varphi U f(x - Ut), \tag{11}$$

implying that for a translating ripple the shape of the local flux will mirror that of the bed height. Furthermore, the ratio $(\partial q/\partial x)/(\varphi \partial h/\partial x)$ will quantify the phase velocity of the ripple. Deviation from this structural correspondence between q and h then represents the growth or decay of the ripple, in the frame traveling with its phase velocity. In particular, a more rapid increase in q near the ripple crest indicates a higher outflux from the crest without a corresponding influx from the stoss side, resulting in a decay of the ripple height. Conversely, a slower growth or reduction in q near the ripple crest indicates a lower outflux from the crest with a higher influx from the stoss side, resulting in a growing ripple. In all the figures to follow, a similar

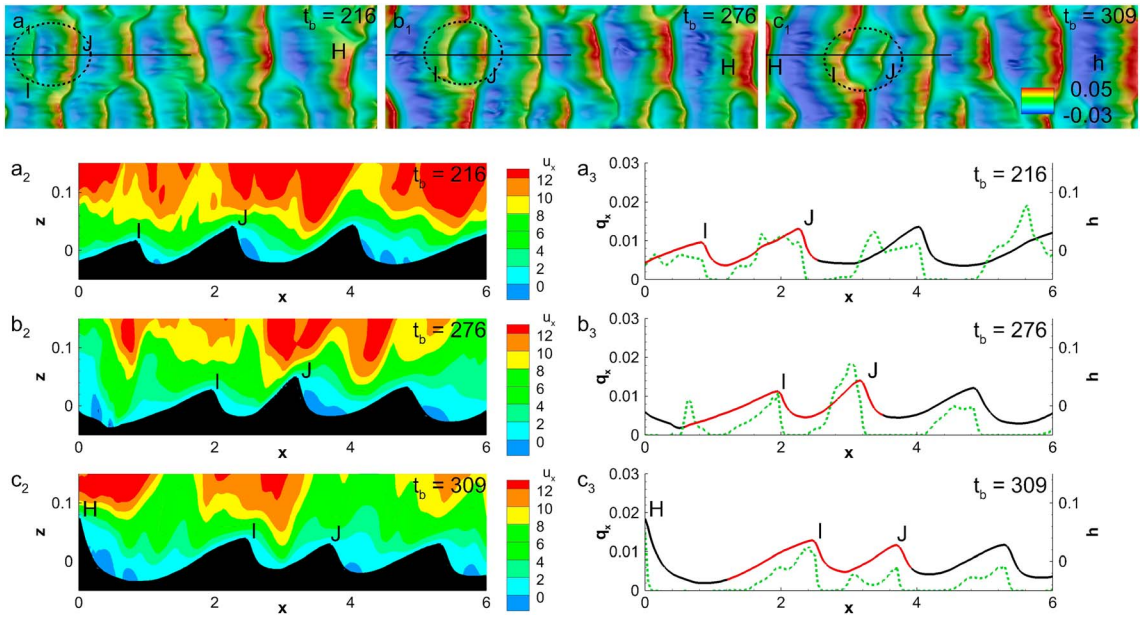

Figure 10. Bedform repulsion from S2. See caption of Figure 9 for details.

balance of sediment influx from the stoss side and outflux from the crest, in the frame of reference moving with the crest, will be used to infer the growth or decay of the ripple.

4.3.3. Bedform Repulsion

The mechanism behind defect repulsion is very similar to that of bedform repulsion shown in Figure 10 (Landry & Werner, 1994; Vermeesch, 2011) but differs in that there are two points of contact between the upstream defect and the downstream bedform (Figure 10 frame b_1). Here again, we consider three time instances, namely, t_b = 216, 276, and 309 corresponding to frames a, b, and c, respectively. The case being considered is that of S2. In the first set of frames, a_1, b_1, and c_1, we show the top view of the bed with iso-contours of elevation. The dashed ellipse points to the interaction under consideration and the straight solid segment represent the spanwise location y = 2.375 as well as the length of the vertical cross-sectional cuts in frames a_2, b_2, and c_2. Note that due to the periodicity of the bed and flow in the streamwise direction, the ripple marked H near the end of the domain at $x \approx 11$ is in fact upstream of the defect marked I at $x \approx 1$. Here we pay special attention to the location of this ripple H upstream of the defect I, where the crest-to-crest separation between the two increases over time (due to the relative size of the bedforms H and I) and remains large enough such that the defect I is unaffected by the upstream ripple H and allowed to grow, or at least maintain its size, over time. Iso-contours of the instantaneous streamwise velocity component u_x demonstrate regions of reverse flow on the lee side of some of the larger ripples. Note that in frame c_3 the large region of near-zero q upstream of bedform I is indicative of a large recirculation region induced by the large ripple H. The upstream defect I is, however, small enough that it does not lead to significant flow reversal on its lee side. However, just as in the case of defect repulsion, it approaches the downstream bedform J and starves the base of its stoss side. Additionally, due to the close proximity of the interacting bedforms I and J, the flow becomes highly erosional on the downstream half of the soon-to-be-repelled bedform J.

The reproducibility of the sequence leading to defect repulsion as well as bedform repulsion shows that this process is not unique but in fact a characteristic of this type of interaction. The mechanism is independent of sediment properties (size, density) and flow parameters, at least for the range of parameters considered in this study, but requires a specific set of conditions to occur: (i) the height and spanwise extent of the upstream defect must be smaller than the downstream structure such that the upstream defect can travel faster, approach the downstream bedform, and repel only the corresponding portion of the downstream bedform. (ii) The defect must be of sufficient height (crest height) such that it is able to locally modify the flow and consequently the sediment flux on its lee side and starve the base of the stoss side of the downstream structure. (iii) The defect must be unaffected by upstream bedforms such that it is allowed to grow as it

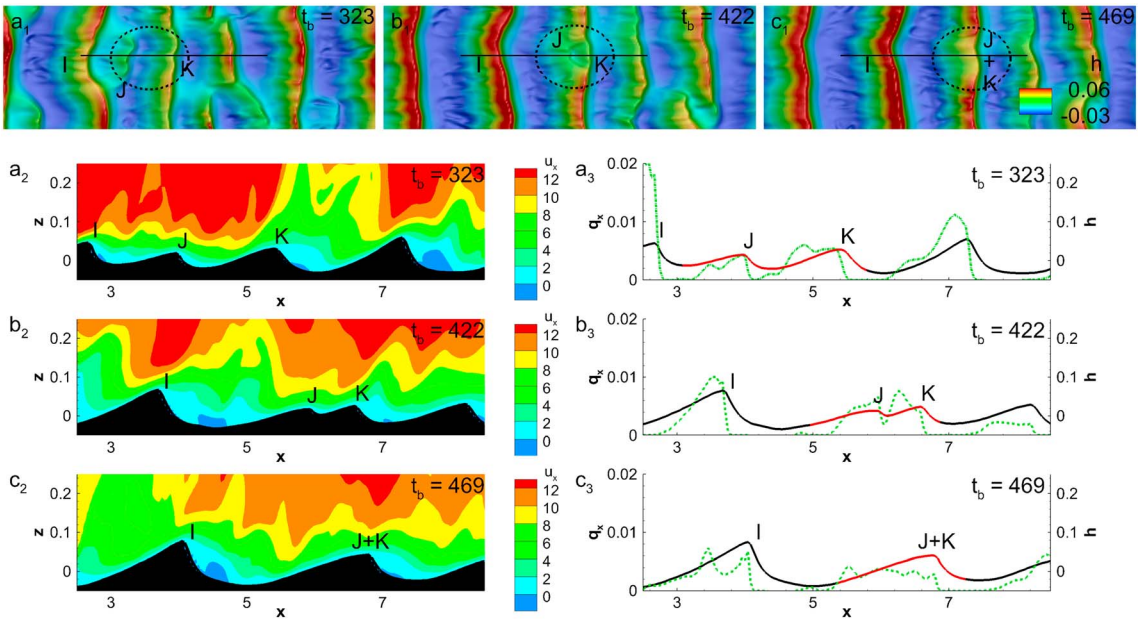

Figure 11. Bedform merging from S2. See caption of Figure 9 for details.

travels downstream. (iv) There must be a sufficient amount of sediment locally available for the defect to grow; that is, a thick enough erodible layer of sediment on the bed must be present. As we will see in the subsequent section, if the second or third condition is not met, a different form of interaction known as bedform merging occurs in lieu of bedform repulsion.

4.3.4. Bedform Merging

Here again, we use a sequence of snapshots to illustrate another form of bedform interaction known as merging (e.g., Mader & Yardley, 1985; Van der Mark et al., 2008; Werner & Kocurek, 1999). Bedform merging as shown in Figure 11 occurs when an upstream smaller and faster defect approaches a downstream larger and slower bedform, but instead of repelling the downstream corresponding portion of the bedform, the defect rides up on the stoss side of the downstream structure until it reaches the crest and merges to form a single structure. The layout and content of the frames used to illustrate this interaction are identical to those in Figure 10 used to demonstrate the process of bedform repulsion. The upstream defect we observe in the merging sequence of Figure 11 in frames a_1, a_2, and a_3 is in fact the same repelled bedform in frames c of Figure 10. As alluded to earlier, the key difference between this sequence and that of bedform repulsion in Figure 10 is the presence of the bedform (marked I) at close proximity to the defect (marked J) on its upstream side. At $t_b = 323$, the crest of this upstream bedform I is located at $x \approx 2.7$. As can be seen from frame a_3, the upstream bedform I starves the defect J by imposing a noneroding flow on the base of its stoss side, which causes the initially smaller defect J to further shrink in size as it travels downstream. The end result is a continually weakening upstream defect (J), with a very narrow nonerodible region on its lee side, incapable of repelling structures. Additionally, the height of the defect J is small enough such that the flow is able to adjust rather smoothly as it passes over its crest. This is apparent from the low and rather uniform q_x value on the stoss side of the downstream bedform as compared to frame b_3 in Figure 10, where the flux is much larger just upstream of the soon-to-be-repelled bedform at $x \approx 3$.

Therefore, if we solely consider the characteristics of the interacting structures without taking into account the presence of upstream neighbors, then our prediction for the outcomes from frames a in Figures 10 and 11 must be matching. Indeed, there is a great deal of similarity at the early stages for these two cases; however, the presence of the upstream bedform at close proximity to the defect in frame a of Figure 11 alters the dynamics of the interaction and results in a different outcome. One should, however, not mistakenly assume that bedform merging only occurs when the defect is being starved by an upstream bedform. If the size of the upstream defect I in Figure 10 were to be much smaller as it approaches the downstream bedform, such that the nonerodible region on the stoss side of the bedform is very narrow (along the flow

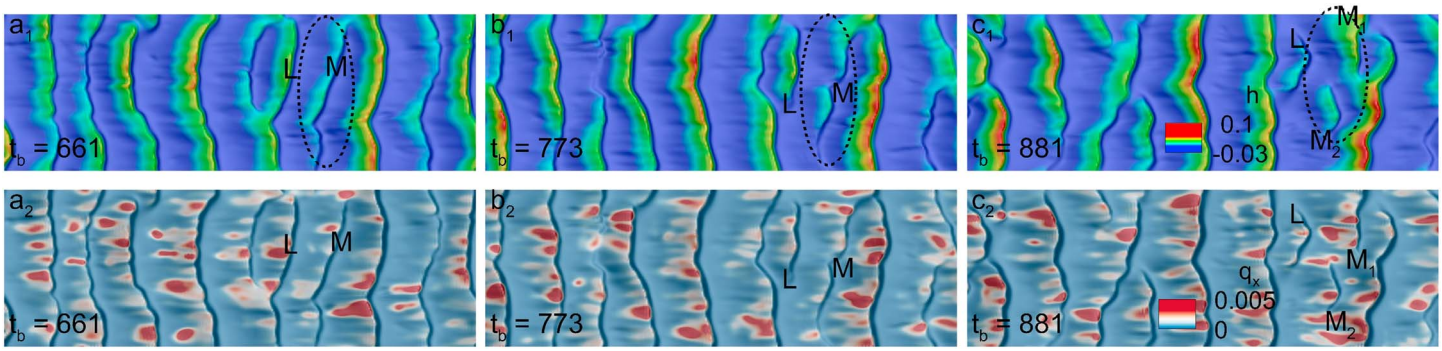

Figure 12. Defect creation from S5. Top three dimensional view with iso-contours of bed elevation (upper frames) and streamwise component of sediment flux (lower frames). Flow is from left to right, and the vertical *z* direction is enlarged by a factor of four for clarity.

direction), and the flow adjusts smoothly to the bed as it passes the crest of the defect, then it is very likely that bedform merging would occur in this case as well.

Therefore, a situation, such as that in Figure 11, where an upstream bedform acts to starve a defect as it approaches another downstream bedform would be very similar to a very small defect, sufficiently far from any upstream structures, approaching a significantly larger downstream bedform.

4.3.5. Defect Creation

Defect creation (Jerolmack & Mohrig, 2005; Parsons & Best, 2013) represents a regenerative interaction where a relatively larger bedform breaks up into smaller structures, otherwise known as defects. An example of defect creation is illustrated in Figure 12. We show a top three-dimensional view of the bed with iso-contours of elevation in the upper set of frames (a_1, b_1, and c_1), and iso-contours of the streamwise volumetric flux of sediment in the lower set of frames (a_2, b_2, and c_2). The case at hand corresponds to S5. At $t_b = 661$, we observe the slightly tilted transverse ripple M within the dashed oval to be relatively uniform along its spanwise direction and to form a coherent structure. Upstream of it, we observe a larger transverse ripple L about to undergo bedform repulsion. The streamwise sediment flux q_x on the portion of the coherent spanwise ripple directly downstream of the soon-to-be-repelled bedform is initially small and uniform for the most part. By $t_b = 773$, bedform repulsion is complete and the repelled bedform now acts to break up the once coherent transverse ripple M. While the repelled bedform L is shorter in the spanwise direction, its crest height is nearly twice as large as that of the downstream ripple M. It therefore seeks to starve and push away the portion of M immediately downstream of it without influencing other portions closer to the lower edge of the frame. This is apparent in frames b_2 and c_2, where q_x is consistently larger on the portion of M downstream of the repelled bedform L. This starvation and repelling process continues and causes the downstream ripple M to split into two defects M_1 and M_2 (frame c_1 and c_2). At $t_b = 881$, we observe the newly created defect M_2, which is closer to the top edge of the frame, to merge with a downstream ripple. We also note that the upper edge of the second newly created defect M_1 is well aligned with the lower edge of the repelled bedform L. This is consistent with the fact that the repelled bedform only influences the portion of the ripple directly downstream of it.

4.4. A Global Description of Bedform Interactions

Bedform interactions in which defects are involved, such as lateral linking, defect and bedform repulsion, defect creation, and merging, usually occur in the early stages of bed evolution, which are characterized by closely spaced, small-scale bedforms, with high defect density (Huntley et al., 2008; Werner & Kocurek, 1999), and consequently high interaction frequency. These interactions are primarily responsible for the constantly evolving bed topology and the accompanying chaotic features. However, bedforms eventually reach a more regular state with low defect density and uniformly spaced bedforms that are similar in size (and migration velocity). During this stage, the frequency of interactions is drastically reduced and the bed approaches a state of near dynamic equilibrium.

Except for the case of lateral linking, the early-time interactions considered herein arise between an upstream defect, of finite spanwise width, and a downstream ripple that spans the width of the computational domain.

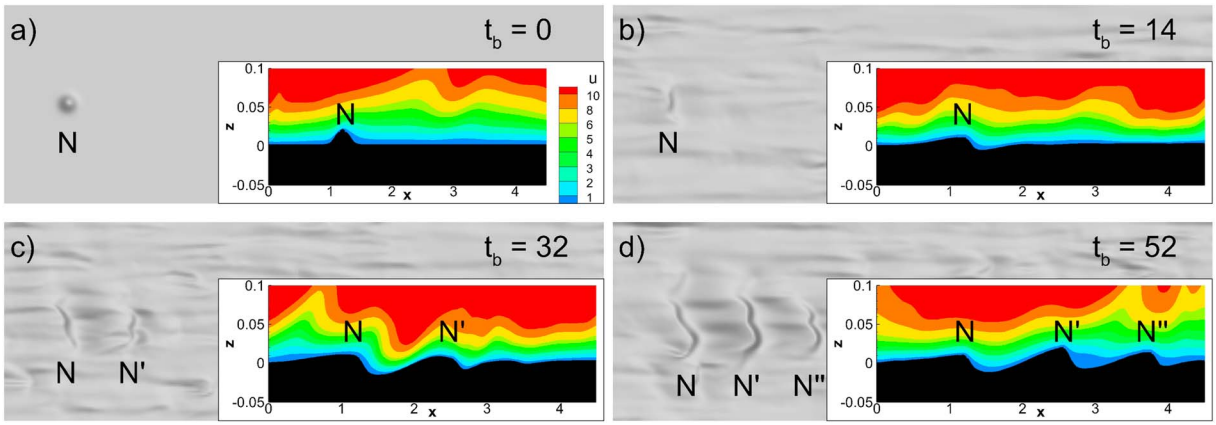

Figure 13. Top three-dimensional view showing the evolution of an isolated sediment pileup (Gaussian bump) from GS1 at four time instances. The bed is circularly shifted in frames b to d to remain in the frame of reference of the pileup at $t_b = 0$, in frame a. Inset: Cross-sectional slice of the bed at $y = 2$ with iso-contours of the instantaneous streamwise component of velocity. Flow is from left to right.

In fact, the mechanism behind these interactions is the same in all cases, but depending on the geometry of interacting structures, namely, the relative height, spanwise extent, and the lateral separation of the centers of bedforms, the interactions are labeled differently. For example, in the cases of defect and bedform repulsion, the main difference is in the spanwise location where the interaction occurs. For bedform repulsion, the interaction occurs well within the spanwise extent (i.e., away from the lateral extremities) of the downstream structure, whereas in the case of defect repulsion, the interaction occurs at one of the lateral sides of the downstream structure. We should also note that bedform interactions also occur when there are changes in forcing conditions.

The upstream bedform is usually the smaller (in height), and hence the faster, of the two interacting structures and thus approaches its downstream neighbor. Once the streamwise separation between the two is small enough, the upstream bedform acts to starve and push away the downstream neighbor. If the upstream bedform is a defect of limited spanwise width, then it only acts on the corresponding portion of its downstream neighbor. Alternatively, if both bedforms span the entire width of the domain, then the interaction will occur across the full span of the bedforms. Moreover, other bedforms, aside from the upstream and downstream neighbors, might indirectly affect the interaction. This was apparent in the cases of bedform repulsion and merging where a bedform upstream of the defect (in the case of bedform merging) played a significant role in determining the outcome of the interaction. The effect of neighboring structures will be discussed in more detail in Paper 2.

5. Evolution of a Sand Pileup

Different theories have been proposed to explain how bedforms initially emerge from a flat bed. One such theory (Coleman & Melville, 1996), derived from experimental observation, suggests that bedforms are initially initiated by the occurrence of random sediment pileups due to the turbulent nature of the flow. These pileups grow by trapping more sediment, become two-dimensional, and when they grow large enough, typically a few sediment grain diameters in height, they generate additional pileups downstream at some preferred wavelength. Coleman and Melville (1996) find this preferred wavelength to depend primarily on grain size and less so on shear velocity.

Numerical simulations are well suited for these types of configurations, which are extremely challenging to arrange experimentally. Indeed, having a sand pileup of only a few grains in height under a turbulent flow is difficult to set up. Consequently, experiments of this type are usually handled by an initial negative defect, that is, an initial cavity in the bed (Perillo, Prokocki, et al., 2014). Figure 13 shows the evolution of such an isolated sediment pileup (Gaussian bump) in the frame of reference of the pileup. That is, each of the frames has been circularly shifted so that the pileup appears stationary as it evolves. The periodic nature of the flow and bed along the streamwise direction allows for such a circular shift. The initial bed height of the Gaussian pileup follows the expression:

Table 4
Geometric Details of the Gaussian Bump Simulations

Simulation number	A_B/d_p	ϵ_B/d_p	Number of bumps	l_{Bx}	l_{By}
GS1	1.94	9.70	1	-	-
GS2	3.88	9.70	1	-	-
GS3	1.94	19.4	1	-	-
GS4	1.94	9.70	2	0	1.0
GS5	1.94	9.70	2	1.2	1.0
GS6	5.82	29.1	1	-	-
GS7	2.74	13.7	1	-	-

Note. A_B corresponds to the maximum height of the bump, and ϵ_B is a measure of the bump's width. For cases GS4 and GS5, for which the domain initially consists of two identical bumps, the separation distance along the x and y directions is denoted by l_{Bx} and l_{By}, respectively.

$$h = A_B \exp\left[-\frac{(x-x_0)^2 + (y-y_0)^2}{2\epsilon_B^2}\right], \tag{12}$$

Here the center of the Gaussian bump is located at (x_0, y_0), A_B represents the maximum height of the Gaussian bump, and ϵ_B is a measure of the width of the bump. Because of the periodicity of the domain in the horizontal directions, only the height and width of the bump are relevant, whereas the exact location of the center is not important. If two identical bumps are present in the domain, the relative separation between the center of the bumps along the streamwise and spanwise directions becomes important.

A total of seven sediment pileup simulations were performed, the details of which are shown in Tables 2 and 4. Similar to all the other cases, this set of simulations is run at a friction Reynolds number of $Re_\tau = 180$, with the same domain size and grid resolution as the other cases. Unlike the S* set of simulations where the sediment bed is initially completely flat, here the sediment bed has a single (cases GS1, GS2, GS3, GS6, and GS7) or a double (cases GS4 and GS5) Gaussian bump midway through the domain. Before the start of each simulation, the bed and consequently the Gaussian bump is held fixed and the turbulent flow was allowed to fully develop and reach a stationary state. Once a stationary state is reached, the bed was allowed to evolve according to the Exner equation (3) starting at $t_b = 0$. In the single bump cases, different dimensions (height and width) of the Gaussian bump, grain size, and flow conditions were varied. The details of which are all listed in Tables 2 and 4. On the other hand, for the double bump simulations, only the separation distance and orientation of the segment joining the centers of the two bumps with respect to the flow were investigated. These resulted in two additional parameters, namely, l_{Bx} and l_{By}, which denote the separation distance between the centers of the bumps along the x and y directions, respectively. Other parameters such as bump dimensions, grain size, and flow conditions were kept unchanged from one case to the other.

Let us start by considering case GS1 and follow the development of that single Gaussian bump. Figure 13 shows the temporal evolution (at four time instances) of the sediment pileup . Here again, vertical structures are exaggerated by stretching the vertical z dimension by a factor of 4 for clarity. In the inset of each frame, we show a cross-sectional cut of the bed at $y = 2$ along with the local and instantaneous streamwise component of velocity. The evolution follows closely the description provided by Coleman and Melville (1996) based on their experimental observations. At $t_b = 0$, the bed is allowed to evolve in response to the local shear stress, where, in the region surrounding the Gaussian bump (marked N), the flow must negotiate its way around this three-dimensional obstacle. Shortly afterward, by $t_b = 14$, the pileup N becomes locally two-dimensional and takes on a shape that closely resembles that of a ripple with a gentle slope on its stoss side and a steeper lee side. The process that causes the Gaussian pileup to become locally two-dimensional is the same as the mechanism discussed in section 4.3.1 that drives chevron features or bedform defects to expand laterally. By $t_b = 32$, the two-dimensional pileup N continues to grow, both laterally and vertically, and in doing so, modifies the flow downstream to generate a second two-dimensional pileup (marked N′) at a spacing of $\lambda_p \approx 1.4$. This process continues so that the newly formed pileup N′ grows and generates yet another two-dimensional pileup N″ at the same downstream spacing of $\lambda_p \approx 1.4$. This preferred spacing is very similar to the separation distance between the crestlines in Figure 3d, which corresponds to case S2 where the initial state of the bed and flow are identical to case GS1, except for the presence of the Gaussian bump. As can be seen from Figure 13, the pileup N only influences the portion of the bed in its immediate downstream vicinity and does not significantly affect sediment transport on its upstream side. Additionally, we observe the stoss side of the initial pileup N in frame d to be relatively flat compared to the stoss sides of the two generated pileups (N′ and N″). This means that the sediment transport along the flow direction during these very early stages is rather uniform on the stoss side of N. This is due to the lack of finite size bedforms upstream of the initial pileup N that acts to accelerate its growth by modifying the flow and enhancing turbulence.

Case GS1 corresponded to a specific set of flow and sediment parameters. To find what effect such parameters have on the development of a small Gaussian bump, we show in Figure 14 a top view of the bed for the other cases in Table 4 at a time when the initial Gaussian bump has generated a second pileup on

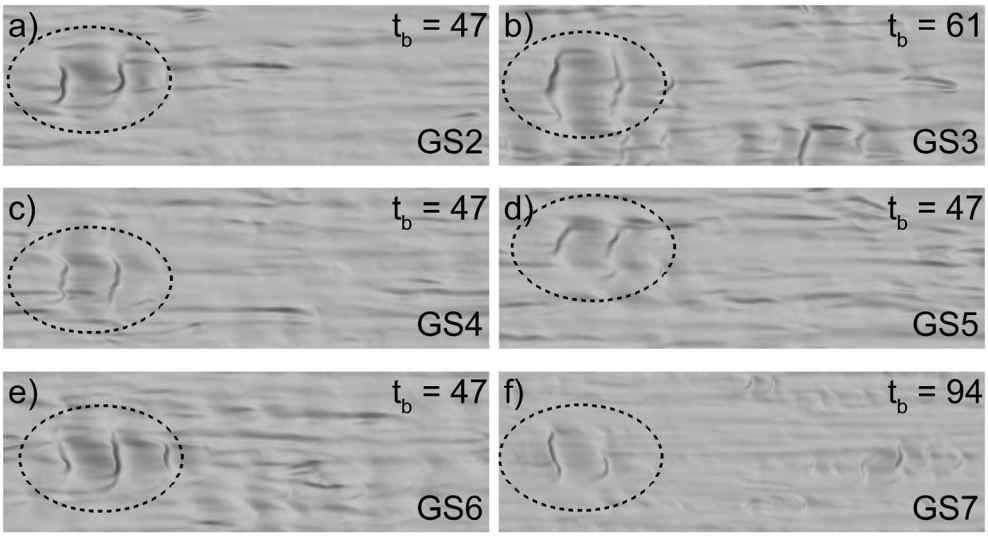

Figure 14. Generation of a downstream pileup at a preferred spacing for the Gaussian bump simulations. The preferred spacing between the generated bump and the initial bump appears to depend marginally on shear velocity and to be independent of bump's geometry and sediment size.

its downstream end. These two pileups are encircled within the dashed ellipse in each frame. The time at which the bed is shown is marked in the upper right corner of each frame along with its corresponding case, in the lower right corner. Case GS2 corresponds to a Gaussian bump whose height (A_B) is twice that for case GS1. For this case, we observe the distance between the two bumps as well as the time at which the second bump emerges to resemble closely those from case GS1. On the other hand, for case GS3, where the height of the Gaussian bump is the same, but ϵ_B is twice as big, we observe the separation distance between the two bumps to be slightly larger. In case GS4, the two pileups are initially aligned normal to the flow with a transverse separation distance between their centers equivalent to the mean flow depth of one nondimensional unit. We observe both bumps to merge and the subsequent dynamics to mirror the aforementioned cases. For case GS5, whose domain also initially comprises of two Gaussian bumps, we observe the upstream bump to generate a pileup that merges with the initial downstream bump. The dynamics again is very similar to the previous cases.

In all the GS* cases we have considered, only the bump's dimensions (height and width) as well as the number of bumps in the domain were modified. In the subsequent two cases, we choose the bump dimensions to correspond to case GS1 and vary the sediment grain diameter (GS6) and shear velocity (GS7), such that the parameters of the latter two cases (see Table 2) correspond to S3 and S5, the initially completely flattened bed cases, respectively. For case GS6, the smaller sediment grain diameter produces an increased volumetric sediment flux, which results in a wavier bed compared to frames a, c, and d, which correspond to the same time in frame e (case GS6), in the initially flattened portion. This is due to the lower shear stress threshold for incipient motion, which results in a larger volumetric flux of sediment. The preferred wavelength is, however, unaffected by the smaller grain size. On the other hand, for the lower shear velocity case GS7, the preferred wavelength of the downstream generated pileup, in nondimensional terms, is slightly smaller than the other cases. We must recall that the flow depth for this case, which is the length scale in the simulations, is about 34% larger than in all the other cases, and therefore in physical space, the preferred wavelength at which the downstream pileup is generated is somewhat larger than in the other cases.

Based on these simulations, λ_p seems to be unaffected by the dimensions of the pileup, as long as it is only a few sediment grain diameters in height and of $O(10)$ sediment grain diameters in width. It is also not affected by the presence of additional pileups at close proximity centered within a radius smaller than the preferred observed spacing. For the different cases in Table 4, we observe from Figure 14 the nondimensional preferred spacing to vary between 1.2 (GS7) and 1.4 (GS1 through GS6).

These results appear to conflict with the findings of Coleman and Melville (1996), where preferred wavelength depends primarily on grain size and to a lesser extent on shear velocity. Their proposed empirical

relation suggests a larger value of $\lambda_p = 3.3$ for all our cases, excluding the smaller grain size case GS6. We note that the physical time to generate the second pileup occurs in less than 10 s for all cases in Table 4. At the rate of wave coarsening observed in case S2, if we were to record the spacing between the bedforms in our simulations at a later time, we would observe a larger value of λ_p, closer to that predicted by Coleman and Melville (1996) (within a few minutes in physical/dimensional time). This perhaps is closer to the observations and recorded measurements in the experimental setup. In fact, Coleman and Melville (1996) do not specify when the measurements were taken during their experiments; however, some of the previous experimental studies (Nakagawa & Tsujimoto, 1984) indicate that the flow in those experiments was stopped and measurements of the wavelength were recorded after the first minute. We need to, however, keep in mind that the present model also involves key assumptions, namely, that the particle-flux is determined locally by the bed shear stress.

The initial conditions and turbulent characteristics in the Gaussian bump case GS1 are identical to those of case S2 except for the presence of the bump. Thus, the bed evolution shown in Figure 13b is qualitatively similar to that in the early evolution of case S2, dominated by streamwise streaks. The most noticeable difference is the incipient crestline formed as a direct consequence of the Gaussian bump. As observed in Figure 3 b, such crestlines naturally form even in the absence of an initial bump, but the formation is significantly delayed. This is consistent with the fact that a larger initial Gaussian bump resulted in a more rapid formation of the crestline. We conjecture that starting from a perfectly flat bed, sand pileups can naturally occur at random locations on the bed, perhaps initiated by intense local turbulent events. These pileups quickly evolve into the cross-stream streak-like patterns seen in Figure 3b (marked A and B). In the Gaussian bump simulations, these streak-like patterns result in the formation of a streamwise train of chevrons, which can be clearly observed in Figure 3c. All the Gaussian bump cases (GS1-GS7), over a long time, follow the sequence presented in Figure 3 and form stable ripple structures.

The Gaussian bump simulations may be used to infer the wavelength of incipient bedforms. As such, the results may be compared to the initial ripple wavelengths obtained from linear stability analysis (e.g., Charru & Mouilleron-Arnould, 2002; Fourrière et al., 2010). For instance, Fourrière et al. (2010) predict the wavelength of the initial ripples to be approximately between 200 and 300 times the grain diameter. While we do not observe a strong dependence between the preferred wavelength and sediment size, we note that the ratio of the preferred wavelength λ_p to sediment diameter obtained in our simulations is around 300, of the same order as the ratio reported by Fourrière et al. (2010).

6. Discussion

Bedform interactions are very common in the process of sediment pattern formation under a shearing flow field. Even though these interactions are driven by the fluid flow, they have been traditionally classified according to the outcome of the sediment pattern with little credit given to the underlying fluid mechanical mechanism, which drives the change through the near bed flow field and consequently the bed shear stress. As illustrated in section 4.3 the underlying mechanisms for many of these bedform interactions are very similar. Therefore, if we were to classify these interactions according to the underlying mechanism and not by the outcome of the sediment pattern, then many of these interactions will fall into a single category. More specifically, the flow-aligned interactions such as defect repulsion, bedform repulsion, bedform merging, and defect creation would essentially be grouped into a set labeled flow aligned interactions. These flow-aligned interactions occur between a smaller (therefore faster) upstream bedform or defect approaching a larger (therefore slower) bedform that is located downstream. Even though the interactions primarily occur between a pair of neighboring bedforms, it is sometimes necessary to include other neighboring bedforms (particularly the farther upstream neighbor) to understand why certain interactions lead to repulsion, while others lead to merging.

Aside from the sediment pattern change induced by these interactions, there is a significant effect to the bedforms involved in the interaction. For a couple of interacting bedforms, the upstream bedform acts to modify the near-bed flow field on the stoss side of the downstream neighbor, and in doing so, it influences the supply chain of sediment along the stoss side. As such, the characteristics of the downstream bedform (such as growth rate and propagation speed) may be impacted. The relation between the bedform celerity and its size may no longer be valid, or at least must be adjusted to account for changes due to the

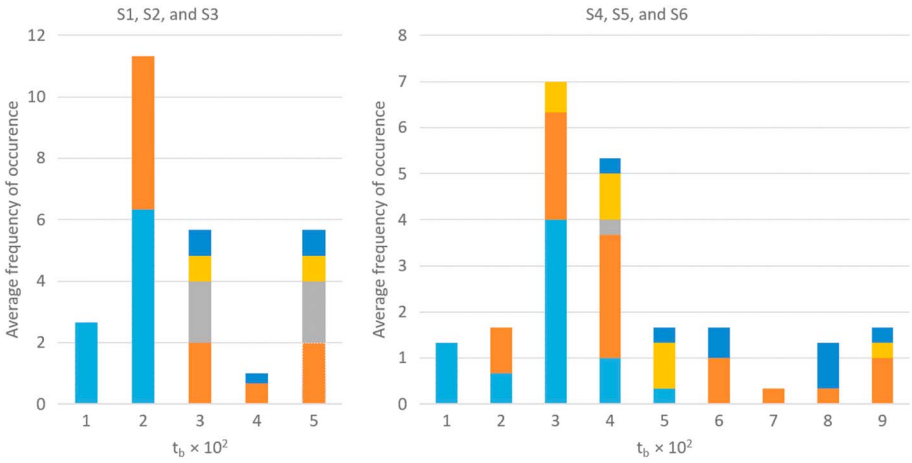

Figure 15. Average frequency of occurrence of bedform interactions. Lateral linking (), defect repulsion (), bedform repulsion (), bedform merging (), and defect creation ().

interaction. In Paper 2, we take a closer look at how these interactions specifically affects the propagation speed and the growth/decay rates of the interacting bedforms.

Certain bedform interactions such as defect and bedform repulsion are a relatively very common feature of bedform dynamics (e.g., Ewing & Kocurek, 2010). We observe these defect-related interactions to be the most prevalent in our simulations. By watching videos (in the supporting information) of bed evolution for each of the six cases S1–S6, we have developed a histogram showing the time, as well as the average frequency, of occurrence of the aforementioned bedform interactions for each of the two sets (S1–S3 and S4–S6). The histogram is shown in Figure 15. The *x* axis corresponds to the time of occurrence and has been discretized into bins of 100 bulk units, and the *y* axis corresponds to the average frequency of occurrence for each of the two sets. For example for cases S4–S6, the third column in the histogram indicates that in a time span ranging from $t_b = 200$ to $t_b = 300$ we have observed a total of 12 lateral linkings, seven defect repulsions, and two bedform mergers in cases S4, S5, and S6. It can be observed from the table that lateral linking is limited to only early time periods during the formation of the ripples, while defect repulsion seems to be the most common bedform dynamics. Morphodynamic systems can be represented as a coupling between flow, sediment transport and bed morphology as illustrated in Figure 16. Spatial and temporal changes in flow conditions, sediment characteristics, sediment transport, linear and nonlinear mechanisms, and large- and small-scale changes in bed topography can be summarized in three main interlinked areas: fluid, sediment transport,

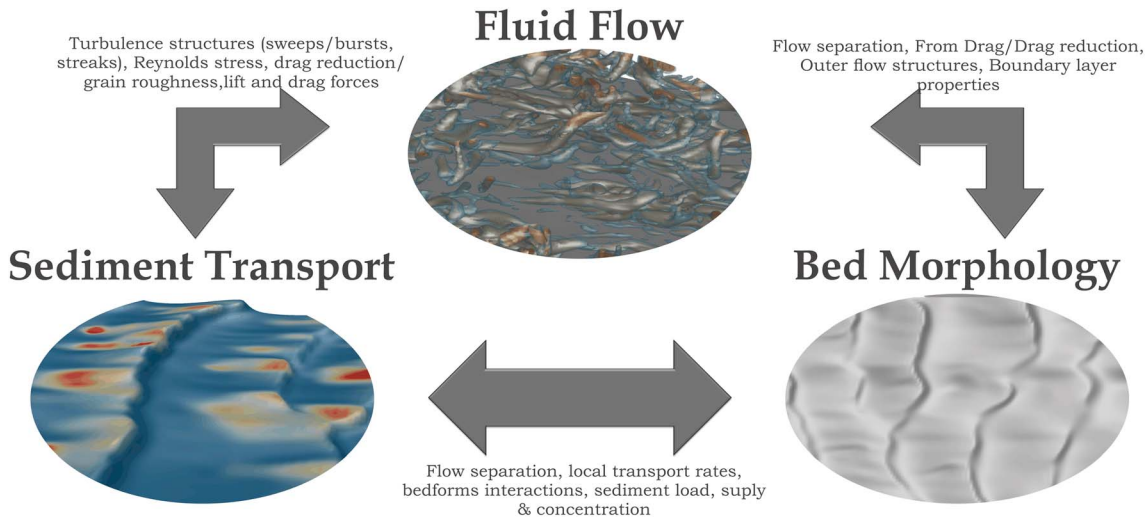

Figure 16. Sedimentological fluid dynamic trinity. A sketch showing the importance of the three components of sedimentological fluid dynamic.

and bed morphology. Hence, all the processes linking flow, sediment transport, and bedform development define the sedimentological fluid dynamic (SFD) "trinity" or morphodynamic processes (Leeder, 1983; Perillo, 2013). In the context of any morphodynamic system, all components of the SFD trinity are connected with the others. Many of the interactions between the elements are inherently nonlinear and time-dependent. This temporal dependence not only needs to take into account the fact that the conditions change over time but also that there may be a lag between the change in one variable and the response of the system (i.e., hysteresis; Dalrymple & Rhodes, 1995). In other words, the different components of the SFD have a particular time-scale within which they react to changes, making it fundamental for all bedform studies to keep track of all of them. For example, water in motion develops turbulent sweeps and bursts that entrain sediment in movement (Heathershaw & Thorne, 1985) and generates differential transport of grains, these areas of erosion and accumulation leading to the generation and development of bedforms (e.g., Venditti et al., 2005). The temporal evolution of the bedform is intrinsically influenced by the magnitude of the sediment transport (e.g., Perillo et al., 2014). Furthermore, as the bedform grows in size it changes the flow and turbulence characteristics, inducing a new condition for transport, which will modify the original bedforms. This is just one example of the many feedback loops that are continually occurring in the vicinity of the bed. It is important to note, that depending on the changes in the flow and sediment transport conditions, the bed topography might require hours, days, or years to readjust.

7. Conclusions

We have presented results from coupled flow-bed simulations for pattern formation under turbulent open channel flow for two scenarios and multiple simulations to study the early stages of ripple formation. The first scenario comprising six simulations was designed to investigate the early evolution of a flat bed. The second scenario involving seven simulations is identical to the first set except for the presence of a single or pair of Gaussian bumps of small amplitude of the order of a grain diameter.

The purpose of the first scenario is to investigate the capability of the simulations in reproducing natural bedform patterns and interactions observed in experiments and field studies. The highly resolved flow field of the simulations facilitated the linking of bedform morphology to the fluid mechanics. We documented a number of bedform interactions including lateral linking, defect and bedform repulsion, defect creation, and bedform merging. For flow-aligned interactions, that is, excluding lateral linking, the underlying mechanisms for most of these interactions are very similar, and the interactions are labeled differently depending on the geometry of interacting structures and the outcome of the interaction. The upstream structure, which is usually the smaller and hence the faster of the interacting structures, approaches its downstream neighbor, then acts to starve and push away the latter. However, other bedforms, aside from the upstream and downstream neighbor, might indirectly affect and change the outcome of the interaction. The effect of neighboring structures will be discussed in greater detail in Paper 2.

The initially chaotic pattern of the erodible bed is due to the strong hairpin and horseshoe-like vortical structures present in the complex turbulent flow field. In the very early stages of pattern formation, these structures leave their imprint on the bed in the form of longitudinal, as well as quasi-spanwise, streaks. This mechanism is identical to the formation of near-wall low-speed streaks in turbulent boundary layers, where the longitudinal streaks of higher bed height were found to be well correlated with local regions of low streamwise velocity (i.e., near-bed low-speed streaks). Additionally, the longitudinal streaks are observed to be highly correlated in the streamwise direction such that they can be several flow depths in length. These vortical structures are of fundamental importance for the initiation of chevron features, which later develop to form crestlines and subsequently ripples. Even though these structures are always present in the flow field and continuously modify the surface of the erodible bed, their effects, with regard to the overall structure of the bed, become of marginal importance in the later stages of pattern formation once bedforms have sufficiently matured. That is once bedform patterns arise, the overlying flow and the sediment transport become functions of bed morphology and the microscale interactions give way to the larger-scale bedform-flow and bedform-bedform interactions. This observation is fully consistent with past observations by Werner (2003) and Kocurek et al. (2010).

The second set of simulations, explored the early time dynamics of bed evolution, characterized by very small length and time scales of the order of a grain diameter and a few seconds, respectively. The simulations also

provide the opportunity to test some of the theories regarding the generation of initial bed waves, such as that of Coleman and Melville (1996) in which they hypothesized that sediment pattern evolution from an initially flattened bed is instigated by the occurrence of small sediment pileups, which grow and generate additional pileups further downstream at a preferred spacing.

Here the erodible bed is initially flattened except for the presence of a Gaussian bump of small amplitude of the order of a grain diameter. The presence of the Gaussian bump mimics the initial sediment pileups, generated by turbulent bursts, which are responsible for the initiation of bedforms. Similar to the experimental finding of Coleman and Melville (1996), the bumps quickly become two-dimensional and generate further pileups downstream of the initial bump at a preferred wavelength. Coleman and Melville (1996) observe this preferred wavelength to scale with particle diameter and proposed an empirical fit relating the two variables. In the present simulations, we do not see such a scaling. The preferred spacing is less than that predicted by the empirical fit of Coleman and Melville (1996) but this may be explained by differences in the experimental time of seconds in the simulation and minutes in the experiment.

Bed evolution in the simulation occurs solely due to bedload transport without allowing for other forms of transport, and thus is applicable to several geophysical situations, where saltation and sediment resuspension are not important due to relatively low values of the excess shear stress on the bed. A wider range of geophysical applications can be addressed in future studies by incorporating saltation and suspension transport mechanisms to the model.

Acknowledgments
We are grateful to ExxonMobil Upstream Research Company for providing support through grant EM09296. Numerical data presented herein will be available in the Sediment Experimentalists Network (SEN) Knowledge Base (http:// www.sedexp.net).

References

Adrian, R. J., Balachandar, S., & Lin, Z. C. (2001). Spanwise growth of vortex structure in wall turbulence. *KSME International Journal*, *15*(12), 1741–1749. https://doi.org/10.1007/BF03185129

Akiki, G., & Balachandar, S. (2016). Immersed boundary method with non-uniform distribution of Lagrangian markers for a non-uniform Eulerian mesh. *Journal of Computational Physics*, *307*, 34–59. https://doi.org/10.1016/j.jcp.2015.11.019

Akiki, G., Jackson, T. L., & Balachandar, S. (2016). Force variation within arrays of monodisperse spherical particles. *Physical Review Fluids*, *1*(4), 044202. https://doi.org/10.1103/PhysRevFluids.1.044202

Akiki, G., Jackson, T. L., & Balachandar, S. (2017). Pairwise interaction extended point-particle model for a random array of monodisperse spheres. *Journal of Fluid Mechanics*, *813*, 882–928. https://doi.org/10.1017/jfm.2016.877

Akiki, G., Moore, W. C., & Balachandar, S. (2017). Pairwise-interaction extended point-particle model for particle-laden flows. *Journal of Computational Physics*, *351*, 329–357. https://doi.org/10.1016/j.jcp.2017.07.056

Ancey, C. (2010). Stochastic modeling in sediment dynamics: Exner equation for planar bed incipient bed load transport conditions. *Journal of Geophysical Research*, *115*, FO0A11. https://doi.org/10.1029/2009JF001260

Anderson, R. S., & McDonald, R. R. (1990). Bifurcations and terminations in eolian ripples. *Eos, Transactions American Geophysical Union*, *71*, 1344.

Andreotti, B., & Claudin, P. (2013). Aeolian and subaqueous bedforms in shear flows. *Philosophical Transactions of the Royal Society A: Mathematical, Physical and Engineering Sciences*, *371*(2004), 20120364. https://doi.org/10.1098/rsta.2012.0364

Ashley, G. M. (1990). Classification of large-scale subaqueous bedforms: A new look at an old problem-SEPM bedforms and bedding structures. *Journal of Sedimentary Research*, *60*(1), 160–172.

Baas, J. H. (1993). Dimensional analysis of current ripples in recent and ancient depositional environments. Ph.D. thesis, Utrecht University, 199 pp.

Baas, J. H. (1994). A flume study on the development and equilibrium morphology of current ripples in very fine sand. *Sedimentology*, *41*(2), 185–209. https://doi.org/10.1111/j.1365-3091.1994.tb01400.x

Baas, A. C. (2007). Complex systems in aeolian geomorphology. *Geomorphology*, *91*(3-4), 311–331. https://doi.org/10.1016/j.geomorph.2007.04.012

Bagnold, R. A., & Taylor, G. (1946). Motion of waves in shallow water. Interaction between waves and sand bottoms. *Proceedings of the Royal Society of London A: Mathematical, Physical and Engineering Sciences*, *187*(1008), 1–18.

Bertin, X., Fortunato, A. B., & Oliveira, A. (2009). A modeling-based analysis of processes driving wave-dominated inlets. *Continental Shelf Research*, *29*(5-6), 819–834. https://doi.org/10.1016/j.csr.2008.12.019

Best, J. (1992). On the entrainment of sediment and initiation of bed defects: Insights from recent developments within turbulent boundary layer research. *Sedimentology*, *39*(5), 797–811. https://doi.org/10.1111/j.1365-3091.1992.tb02154.x

Best, J. L. (1993). On the interactions between turbulent flow structure, sediment transport and bedform development: Some considerations from recent experimental research. In N. Clifford, J. French, & J. Hardisty (Eds.), *Turbulence: Perspectives on Flow and Sediment Transport*, (pp. 61–92). Chichester, New York: John Wiley.

Best, J. (2005). The fluid dynamics of river dunes: A review and some future research directions. *Journal of Geophysical Research*, *110*, F04S02. https://doi.org/10.1029/2004JF000218

Best, J., & Kostaschuk, R. (2002). An experimental study of turbulent flow over a low-angle dune. *Journal of Geophysical Research*, *107*(C9), 3135. https://doi.org/10.1029/2000JC000294

Breed, C. S., Grolier, M. J., & McCauley, J. F. (1979). Morphology and distribution of common 'sand'dunes on Mars: Comparison with the Earth. *Journal of Geophysical Research*, *84*(B14), 8183–8204. https://doi.org/10.1029/JB084iB14p08183

Cantero, M. I., Balachandar, S., Cantelli, A., Pirmez, C., & Parker, G. (2009). Turbidity current with a roof: Direct numerical simulation of self-stratified turbulent channel flow driven by suspended sediment. *Journal of Geophysical Research*, *114*, C03008. https://doi.org/10.1029/2008JC004978

Cantero, M. I., Balachandar, S., & Garcia, M. H. (2007). High-resolution simulations of cylindrical density currents. *Journal of Fluid Mechanics*, *590*, 437–469.

Cayocca, F. (2001). Long-term morphological modeling of a tidal inlet: The Arcachon Basin, France. *Coastal Engineering*, *42*(2), 115–142. https://doi.org/10.1016/S0378-3839(00)00053-3

Chakraborty, P., Balachandar, S., & Adrian, R. J. (2005). On the relationships between local vortex identification schemes. *Journal of Fluid Mechanics*, *535*, 189–214. https://doi.org/10.1017/S0022112005004726

Charru, F., Andreotti, B., & Claudin, P. (2013). Sand ripples and dunes. *Annual Review of Fluid Mechanics*, *45*(1), 469–493. https://doi.org/10.1146/annurev-fluid-011212-140806

Charru, F., Bouteloup, J., Bonometti, T., & Lacaze, L. (2016). Sediment transport and bedforms: A numerical study of two-phase viscous shear flow. *Meccanica*, *51*(12), 3055–3065. https://doi.org/10.1007/s11012-016-0553-5

Charru, F., & Mouilleron-Arnould, H. (2002). Instability of a bed of particles sheared by a viscous flow. *Journal of Fluid Mechanics*, *452*, 303–323.

Chou, Y. J., & Fringer, O. B. (2010). A model for the simulation of coupled flow-bed form evolution in turbulent flows. *Journal of Geophysical Research*, *115*, C10041. https://doi.org/10.1029/2010JC006103

Coco, G., & Murray, A. B. (2007). Patterns in the sand: From forcing templates to self-organization. *Geomorphology*, *91*(3-4), 271–290. https://doi.org/10.1016/j.geomorph.2007.04.023

Coleman, S. E., Fedele, J. J., & Garcia, M. H. (2003). Closed-conduit bed-form initiation and development. *Journal of Hydraulic Engineering*, *129*(12), 956–965. https://doi.org/10.1061/(ASCE)0733-9429(2003)129:12(956)

Coleman, S. E., & Fenton, J. D. (2000). Potential-flow instability theory and alluvial stream bed forms. *Journal of Fluid Mechanics*, *418*, 101–117. https://doi.org/10.1017/S0022112000001099

Coleman, S. E., & Melville, B. W. (1994). Bed-form development. *Journal of Hydraulic Engineering*, *120*(5), 544–560. https://doi.org/10.1061/(ASCE)0733-9429(1994)120:5(544)

Coleman, S. E., & Melville, B. W. (1996). Initiation of bed forms on a flat sand bed. *Journal of Hydraulic Engineering*, *122*(6), 301–310. https://doi.org/10.1061/(ASCE)0733-9429(1996)122:6(301)

Colombini, M. (2004). Revisiting the linear theory of sand dune formation. *Journal of Fluid Mechanics*, *502*, 1–16. https://doi.org/10.1017/S0022112003007201

Cortese, T. A., & Balachandar, S. (1995). High performance spectral simulation of turbulent flows in massively parallel machines with distributed memory. *International Journal of High Performance Computing Applications*, *9*(3), 187–204. https://doi.org/10.1177/109434209500900302

Dalrymple, R. W., & Rhodes, R. N. (1995). Estuarine dunes and bars. *Developments in Sedimentology*, *53*, 359–422. https://doi.org/10.1016/S0070-4571(05)80033-0

De Angelis, V., Lombardi, P., & Banerjee, S. (1997). Direct numerical simulation of turbulent flow over a wavy wall. *Physics of Fluids*, *9*(8), 2429–2442. https://doi.org/10.1063/1.869363

Elbelrhiti, H., Andreotti, B., & Claudin, P. (2008). Barchan dune corridors: Field characterization and investigation of control parameters. *Journal of Geophysical Research*, *113*, F02S15. https://doi.org/10.1029/2007JF000767

Endo, N., Taniguchi, K., & Katsuki, A. (2004). Observation of the whole process of interaction between barchans by flume experiments. *Geophysical Research Letters*, *31*, L12503. https://doi.org/10.1029/2004GL020168

Engelund, F. (1970). Instability of erodible beds. *Journal of Fluid Mechanics*, *42*(02), 225–244. https://doi.org/10.1017/S0022112070001210

Engelund, F., & Fredsoe, J. (1982). Sediment ripples and dunes. *Annual Review of Fluid Mechanics*, *14*(1), 13–37. https://doi.org/10.1146/annurev.fl.14.010182.000305

Escauriaza, C., & Sotiropoulos, F. (2011). Initial stages of erosion and bed form development in a turbulent flow around a cylindrical pier. *Journal of Geophysical Research*, *116*, F03007. https://doi.org/10.1029/2010JF001749

Ewing, R. C., & Kocurek, G. A. (2010). Aeolian dune interactions and dune-field pattern formation: White Sands Dune Field, New Mexico. *Sedimentology*, *57*(5), 1199–1219.

Fedele, J., & García, M. (2009). Laboratory experiments on the formation of subaqueous depositional gullies by turbidity currents. *Marine Geology*, *258*(1-4), 48–59. https://doi.org/10.1016/j.margeo.2008.11.004

Fedele, J., Hoyal, D., Barnaal, Z., & Awalt, S. (2014). Experiments on bedforms created by gravity flows. EGU General Assembly Conference Abstracts (Vol. 16, p. 4514).

Fedele, J. J., Hoyal, D., Barnaal, Z., Tulenko, J., & Awalt, S. (2016). Autogenic dynamics and self-organization in sedimentary systems. SEPM Special Publication (Vol. 106). https://doi.org/10.2110/sepmsp.106.12

Fourrière, A., Claudin, P., & Andreotti, B. (2010). Bedforms in a turbulent stream: Formation of ripples by primary linear instability and of dunes by nonlinear pattern coarsening. *Journal of Fluid Mechanics*, *649*, 287–328. https://doi.org/10.1017/S0022112009993466

Garcia, M. (2008). Sediment transport and morphodynamics. In *Review of Sedimentation Engineering: Processes, Measurements, Modeling, and Practice*, *ASCE Manuals and Reports on Engineering Practice*, (Vol. 110, pp. 21–163). Reston, VA: American Society of Civil Engineers. https://doi.org/10.1061/9780784408148.ch02

Giri, S., & Shimizu, Y. (2006). Numerical computation of sand dune migration with free surface flow. *Water Resources Research*, *42*, W10422. https://doi.org/10.1029/2005WR004588

Guérin, T., Bertin, X., & Dodet, G. (2016). A numerical scheme for coastal morphodynamic modelling on unstructured grids. *Ocean Modelling*, *104*, 45–53. https://doi.org/10.1016/j.ocemod.2016.04.009

Gyr, A., & Schmid, A. (1997). Turbulent flows over smooth erodible sand beds in flumes. *Journal of Hydraulic Research*, *35*(4), 525–544. https://doi.org/10.1080/00221689709498409

Heathershaw, A. D., & Thorne, P. D. (1985). Sea-bed noises reveal role of turbulent bursting phenomenon in sediment transport by tidal currents. *Nature*, *316*(6026), 339–342. https://doi.org/10.1038/316339a0

Hersen, P., Andersen, K. H., Elbelrhiti, H., Andreotti, B., Claudin, P., & Douady, S. (2004). Corridors of barchan dunes: Stability and size selection. *Physical Review E*, *69*(1), 011304. https://doi.org/10.1103/PhysRevE.69.011304

Hersen, P., & Douady, S. (2005). Collision of barchan dunes as a mechanism of size regulation. *Geophysical Research Letters*, *32*, L21403. https://doi.org/10.1029/2005GL024179

Hino, M. (1968). Equilibrium-range spectra of sand waves formed by flowing water. *Journal of Fluid Mechanics*, *34*(03), 565–573. https://doi.org/10.1017/S0022112068002089

Howard, A. D. (2007). Simulating the development of Martian highland landscapes through the interaction of impact cratering, fluvial erosion, and variable hydrologic forcing. *Geomorphology*, *91*(3-4), 332–363. https://doi.org/10.1016/j.geomorph.2007.04.017

Huntley, D. A., Coco, G., Bryan, K. R., & Murray, A. B. (2008). Influence of "defects" on sorted bedform dynamics. *Geophysical Research Letters*, *35*, L02601. https://doi.org/10.1029/2007GL030512

Jerolmack, D. J., & Mohrig, D. (2005). A unified model for subaqueous bed form dynamics. *Water Resources Research*, *41*, W12421. https://doi.org/10.1029/2005WR004329

Kennedy, J. F. (1969). The formation of sediment ripples, dunes, and antidunes. *Annual Review of Fluid Mechanics*, *1*(1), 147–168. https://doi.org/10.1146/annurev.fl.01.010169.001051

Khosronejad, A., Kang, S., Borazjani, I., & Sotiropoulos, F. (2011). Curvilinear immersed boundary method for simulating coupled flow and bed morphodynamic interactions due to sediment transport phenomena. *Advances in Water Resources*, *34*(7), 829–843. https://doi.org/10.1016/j.advwatres.2011.02.017

Kidanemariam, A. G., & Uhlmann, M. (2014). Direct numerical simulation of pattern formation in subaqueous sediment. *Journal of Fluid Mechanics*, *750*, R2. https://doi.org/10.1017/jfm.2014.284

Kidanemariam, A. G., & Uhlmann, M. (2017). Formation of sediment patterns in channel flow: Minimal unstable systems and their temporal evolution. *Journal of Fluid Mechanics*, *818*, 716–743.

Kocurek, G., & Ewing, R. C. (2005). Aeolian dune field self-organization–implications for the formation of simple versus complex dune-field patterns. *Geomorphology*, *72*(1-4), 94–105. https://doi.org/10.1016/j.geomorph.2005.05.005

Kocurek, G., Ewing, R. C., & Mohrig, D. (2010). How do bedform patterns arise? New views on the role of bedform interactions within a set of boundary conditions. *Earth Surface Processes and Landforms*, *35*(1), 51–63. https://doi.org/10.1002/esp.1913

Kocurek, G., Townsley, M., Yeh, E., Havholm, K., & Sweet, M. L. (1992). Dune and dune-field development on Padre Island, Texas, with implications for interdune deposition and water-table-controlled accumulation. *Journal of Sedimentary Research*, *62*(4), 622–635.

Kostaschuk, R. (2000). A field study of turbulence and sediment dynamics over subaqueous dunes with flow separation. *Sedimentology*, *47*(3), 519–531. https://doi.org/10.1046/j.1365-3091.2000.00303.x

Kostic, S., Sequeiros, O., Spinewine, B., & Parker, G. (2010). Cyclic steps: A phenomenon of supercritical shallow flow from the high mountains to the bottom of the ocean. *Journal of Hydro-Environment Research*, *3*(4), 167–172. https://doi.org/10.1016/j.jher.2009.10.002

Landry, W., & Werner, B. T. (1994). Computer simulations of self-organized wind ripple patterns. *Physica D: Nonlinear Phenomena*, *77*(1-3), 238–260. https://doi.org/10.1016/0167-2789(94)90137-6

Leeder, M. R. (1983). On the interactions between turbulent flow, sediment transport and bedform mechanics in channelized flows. *Modern and Ancient Fluvial Systems*, *6*, 5–18.

Mader, D., & Yardley, M. J. (1985). Migration, modification and merging in aeolian systems and the significance of the depositional mechanisms in Permian and Triassic dune sands of Europe and North America. *Sedimentary Geology*, *43*(1-4), 85–218. https://doi.org/10.1016/0037-0738(85)90056-9

McLean, S. R. (1990). The stability of ripples and dunes. *Earth-Science Reviews*, *29*(1-4), 131–144. https://doi.org/10.1016/0012-8252(0)90032-Q

Meyer-Peter, E., & Müller, R. (1948). Formulas for bed-load transport. IAHSR 2nd meeting, Stockholm, appendix 2. IAHR.

Müller, A., & Gyr, A. (1986). On the vortex formation in the mixing layer behind dunes. *Journal of Hydraulic Research*, *24*(5), 359–375. https://doi.org/10.1080/00221688609499314

Nabi, M., Vriend, H. J., Mosselman, E., Sloff, C. J., & Shimizu, Y. (2013). Detailed simulation of morphodynamics: 3. Ripples and dunes. *Water Resources Research*, *49*, 5930–5943. https://doi.org/10.1002/wrcr.20457

Nakagawa, H., & Tsujimoto, T. (1984). Spectral analysis of sand bed instability. *Journal of Hydraulic Engineering*, *110*(4), 467–483. https://doi.org/10.1061/(ASCE)0733-9429(1984)110:4(467)

Nelson, J. M., & Smith, J. D. (1989). Mechanics of flow over ripples and dunes. *Journal of Geophysical Research*, *94*(C6), 8146–8162. https://doi.org/10.1029/JC094iC06p08146

Nielsen, P. (1981). Dynamics and geometry of wave-generated ripples. *Journal of Geophysical Research*, *86*(C7), 6467–6472. https://doi.org/10.1029/JC086iC07p06467

Niemann, S. L., Fredsøe, J., & Jacobsen, N. G. (2010). Sand dunes in steady flow at low Froude numbers: Dune height evolution and flow resistance. *Journal of Hydraulic Engineering*, *137*(1), 5–14.

Ouriemi, M., Aussillous, P., & Guazzelli, E. (2009a). Sediment dynamics. Part 1. Bed-load transport by laminar shearing flows. *Journal of Fluid Mechanics*, *636*, 295–319. https://doi.org/10.1017/S0022112009007915

Ouriemi, M., Aussillous, P., & Guazzelli, E. (2009b). Sediment dynamics. Part 2. Dune formation in pipe flow. *Journal of Fluid Mechanics*, *636*, 321–336. https://doi.org/10.1017/S0022112009007927

Paarlberg, A. J., Dohmen-Janssen, C. M., Hulscher, S. J., & Termes, P. (2009). Modeling river dune evolution using a parameterization of flow separation. *Journal of Geophysical Research*, *114*, F01014. https://doi.org/10.1029/2007JF000910

Paola, C., & Voller, V. R. (2005). A generalized Exner equation for sediment mass balance. *Journal of Geophysical Research*, *110*, F04014. https://doi.org/10.1029/2004JF000274

Parsons, D. R., & Best, J. (2013). Bedforms: Views and new perspectives from the third international workshop on Marine and River Dune Dynamics (MARID3). *Earth Surface Processes and Landforms*, *38*(3), 319–329. https://doi.org/10.1002/esp.3360

Perillo, M.M. (2013). Flow, sediment transport and bedforms under combined-flows. Ph.D. thesis, University of Illinois at Urbana-Champaign, 177 pp.

Perillo, M. M., Best, J. L., & Garcia, M. H. (2014). A new phase diagram for combined-flow bedforms. *Journal of Sedimentary Research*, *84*(4), 301–313. https://doi.org/10.2110/jsr.2014.25

Perillo, M. M., Best, J. L., Yokokawa, M., Sekiguchi, T., Takagawa, T., & Garcia, M. H. (2014). A unified model for bedform development and equilibrium under unidirectional, oscillatory and combined-flows. *Sedimentology*, *61*(7), 2063–2085. https://doi.org/10.1111/sed.12129

Perillo, M. M., Prokocki, E. W., Best, J. L., & Garcia, M. H. (2014). Bed form genesis from bed defects under unidirectional, oscillatory, and combined flows. *Journal of Geophysical Research: Earth Surface*, *119*, 2635–2652. https://doi.org/10.1002/2014JF003167

Ribberink, J. S., & Al-Salem, A. A. (1994). Sediment transport in oscillatory boundary layers in cases of rippled beds and sheet flow. *Journal of Geophysical Research*, *99*(C6), 12,707–12,727. https://doi.org/10.1029/94JC00380

Richards, K. J. (1980). The formation of ripples and dunes on an erodible bed. *Journal of Fluid Mechanics*, *99*(03), 597–618. https://doi.org/10.1017/S002211208000078X

Sharp, R. P. (1963). Wind ripples. *The Journal of Geology*, *71*(5), 617–636.

Shields, A. (1936). *Application of similarity principles and turbulence research to bed-load movement*. Pasadena, CA: Soil Conservation Service, California Institute of Technology.

Shringarpure, M., Cantero, M. I., & Balachandar, S. (2012). Dynamics of complete turbulence suppression in turbidity currents driven by monodisperse suspensions of sediment. *Journal of Fluid Mechanics*, *712*, 384–417. https://doi.org/10.1017/jfm.2012.427

Smith, I. B., Holt, J. W., Spiga, A., Howard, A. D., & Parker, G. (2013). The spiral troughs of Mars as cyclic steps. *Journal of Geophysical Research: Planets*, *118*, 1835–1857. https://doi.org/10.1002/jgre.20142

Sotiropoulos, F., & Khosronejad, A. (2016). Sand waves in environmental flows: Insights gained by coupling large-eddy simulation with morphodynamics. *Physics of Fluids*, *28*(2), 021301. https://doi.org/10.1063/1.4939987

Stam, J. M. T. (1997). On the modelling of two-dimensional aeolian dunes. *Sedimentology*, *44*(1), 127–141. https://doi.org/10.1111/j.1365-3091.1997.tb00428.x

Sun, R., & Xiao, H. (2016). CFD–DEM simulations of current-induced dune formation and morphological evolution. *Advances in Water Resources*, *92*, 228–239. https://doi.org/10.1016/j.advwatres.2016.03.018

Swanson, T., Mohrig, D., Kocurek, G., & Liang, M. (2016). A surface model for aeolian dune topography. *Mathematical Geosciences*, 1–21.

Uhlmann, M. (2005). An immersed boundary method with direct forcing for the simulation of particulate flows. *Journal of Computational Physics*, *209*(2), 448–476. https://doi.org/10.1016/j.jcp.2005.03.017

Van der Mark, C. F., Blom, A., & Hulscher, S. J. M. H. (2008). Quantification of variability in bedform geometry. *Journal of Geophysical Research*, *113*, F03020. https://doi.org/10.1029/2007JF000940

Venditti, J. G., Church, M. A., & Bennett, S. J. (2005). Bed form initiation from a flat sand bed. *Journal of Geophysical Research*, *110*, F01009. https://doi.org/10.1029/2004JF000149

Vermeesch, P. (2011). Solitary wave behavior in sand dunes observed from space. *Geophysical Research Letters*, *38*, L22402. https://doi.org/10.1029/2011GL049610

Werner, B. T. (1995). Eolian dunes: Computer simulations and attractor interpretation. *Geology*, *23*(12), 1107–1110. https://doi.org/10.1130/0091-7613(1995)023<1107:EDCSAA>2.3.CO;2

Werner, B. T. (1999). Complexity in natural landform patterns. *Science*, *284*(5411), 102–104. https://doi.org/10.1126/science.284.5411.102

Werner, B. T. (2003). Modeling landforms as self-organized, hierarchical dynamical systems. *Prediction in Geomorphology*, 133–150.

Werner, B. T., & Kocurek, G. (1997). Bed-form dynamics: Does the tail wag the dog? *Geology*, *25*(9), 771–774. https://doi.org/10.1130/0091-7613(1997)025<0771:BFDDTT>2.3.CO;2

Werner, B. T., & Kocurek, G. (1999). Bedform spacing from defect dynamics. *Geology*, *27*(8), 727–730. https://doi.org/10.1130/0091-7613(1999)027<0727:BSFDD>2.3.CO;2

Wilson, I. G. (1972). Aeolian bedforms—Their development and origins. *Sedimentology*, *19*(3-4), 173–210. https://doi.org/10.1111/j.1365-3091.1972.tb00020.x

Wong, M., & Parker, G. (2006). Reanalysis and correction of bed-load relation of Meyer-Peter and Müller using their own database. *Journal of Hydraulic Engineering*, *132*(11), 1159–1168. https://doi.org/10.1061/(ASCE)0733-9429(2006)132:11(1159)

Zgheib, N., Bonometti, T., & Balachandar, S. (2015a). Direct numerical simulation of cylindrical particle-laden gravity currents. *Computers & Fluids*, *123*, 23–31. https://doi.org/10.1016/j.compfluid.2015.09.001

Zgheib, N., Bonometti, T., & Balachandar, S. (2015b). Propagation and deposition of non-circular finite release particle-laden currents. *Physics of Fluids*, *27*(8), 086604. https://doi.org/10.1063/1.4929397

Zgheib, N., Fedele, J. J., Hoyal, D. C. J. D., Perillo, M. M., & Balachandar, S. (2018). Direct numerical simulation of transverse ripples: 2. Self-similarity, bedform coarsening, and effect of neighboring structures. *Journal of Geophysical Research: Earth Surface*, *123*. https://doi.org/10.1002/2017JF004399

Zhou, J., Adrian, R. J., & Balachandar, S. (1996). Autogeneration of near-wall vortical structures in channel flow. *Physics of Fluids*, *8*(1), 288–290. https://doi.org/10.1063/1.868838

Zhou, J., Adrian, R. J., Balachandar, S., & Kendall, T. M. (1999). Mechanisms for generating coherent packets of hairpin vortices in channel flow. *Journal of Fluid Mechanics*, *387*, 353–396. https://doi.org/10.1017/S002211209900467X